atmosphere MDPI

Article

Evaluation of Rain Estimates from Several Ground-Based Radar Networks and Satellite Products for Two Cases Observed over France in 2022

Antoine Causse [1,2,*], **Céline Planche** [1,3], **Emmanuel Buisson** [2] and **Jean-Luc Baray** [1,*]

[1] Université Clermont Auvergne, Centre National de la Recherche Scientifique (CNRS), Laboratoire de Météorologie Physique, UMR 6105, F63000 Clermont-Ferrand, France; celine.planche@uca.fr
[2] Weather-Measures, F63000 Clermont-Ferrand, France; emmanuel.buisson@weather-measures.com
[3] Institut Universitaire de France (IUF)
* Correspondence: antoine.causse63@gmail.com (A.C.); j-luc.baray@uca.fr (J.-L.B.)

Abstract: The recent development of satellite products for observing precipitation based on different technologies (microwaves, infrared, etc.) allows for near-real-time meteorological studies. The purpose of this article is to evaluate 11 satellite products (GHE, PDIR, IMERG-Early v6, IMERG-Late v6, CMORPH v0.x, CMORPH-RT v0.x, GSMaP-NRT v7, GSMaP-NRT-GC v7, GSMaP-NOW v7, GSMaP-NOW-GC v7, and DATABOURG) currently available and compare them to 2 ground-based radar networks (PANTHERE and OPERA) and the French rain-gauge network RADOME. Two case studies of intense precipitation over France (22 to 25 April 2022 and 24 to 29 June 2022) were selected. The radar estimations are closer to the RADOME observations than the satellite-based estimations, which tend to globally underestimate the precipitation amounts over the areas of interest while OPERA tends to strongly overestimate precipitation amounts during the June case study. The PANTHERE radar product and the carrier-to-noise product DATABOURG shows promising results. Near-real-time satellite products tend to have closer precipitation amounts to the reference dataset than satellite products with a shorter latency. The use of these datasets for nowcasting developments is plausible but further analyses must be conducted beforehand.

Keywords: precipitation; remote sensing; radars; satellite

check for updates

Citation: Causse, A.; Planche, C.; Buisson, E.; Baray, J.-L. Evaluation of Rain Estimates from Several Ground-Based Radar Networks and Satellite Products for Two Cases Observed over France in 2022. *Atmosphere* **2023**, *14*, 1726. https://doi.org/10.3390/atmos14121726

Academic Editors: Dabin Ji, Shihao Tang, Ziqiang Ma, Wei Li and Yingzhao Ma

Received: 27 October 2023
Revised: 17 November 2023
Accepted: 20 November 2023
Published: 24 November 2023

1. Introduction

Precipitation is an important part of the water cycle, and it drives the supply of water resources for the agriculture, industry, and even society as a whole [1]. Intense rainfall can trigger floods causing life-threatening situations [2,3], and a lack of precipitation induces droughts [4], impacting the agricultural sector. The successive reports published by the Intergovernmental Panel on Climate Change [5] show that a warmer global climate will increase the number and intensity of extreme episodes, such as droughts and intense precipitations. Ren et al. [6] have already observed a slight increase in precipitation over land at a global scale since the beginning of the 20th century and of extreme precipitation events at the local scale. Over Europe, the number of extreme flood events has increased by 0.3% per year over the period from 1870 to 2016 [7]. Moreover, the observed precipitation fields at high spatial and temporal resolution can be used as inputs for meteorological, climatic, and hydrological numerical studies [8]. The monitoring of precipitation can be used to assess landslide and slope failure risks over mountainous areas [9,10].

Precipitation estimates at near-real-time can be provided by three categories of instruments: rain-gauge networks, ground-based weather radars, and remote sensing facilities onboard satellites. Rain gauges permit the quantification of surface-rain amounts locally [11] and, structured in networks, they can provide sparse information on the spatial and temporal distributions of precipitation [1]. However, rain gauges cannot be installed over seas and oceans. The data coverage can be spaced out in sparsely populated areas, which is a limitation for global- or large-scale studies [12]. Weather radar provides useful information about the rain rate at a high spatial and temporal resolution. Nevertheless, as for the rain gauges, they cannot be installed over marine surfaces. Projects based on radar networks allow for the building of rain-products over larger areas, such as over France (PANTHERE project; [13]) or Europe (OPERA project; [14]). Note that all the acronyms used in this paper are defined in the Abbreviations.

Largely developed in recent years, remote sensing observations from satellites have enabled improvements in precipitation estimates on a large spatial scale. Different sensors are used to estimate precipitation amounts: infrared (IR) or visible (VIS), and passive or active microwave (PMW or AMW) sensors. The IR and VIS observations are often used aboard geostationary (GEO) satellites [1], while AMW and PMW sensors are deployed in a constellation of Low Earth Orbiting (LEO) satellites which only cover a swath of the Earth's surface [15]. Commonly, the GEO-IR sensors measure the cloud-top brightness temperature (T_b) and, thanks to empirical relationships, can estimate rain rates at the surface. LEO-PMW radiometers measure the effect of large liquid and ice particles on the upwelling radiation coming from the Earth's surface to estimate rain rate [1], whereas spaceborne precipitation radars, called LEO-AMW sensors, use the information retrieved by the backscatter signal from rain-sized particles. Moreover, GEO-IR sensors permit the study of a unique part of the world with a high spatiotemporal resolution and can estimate the rain rates derived from cloud-top brightness temperature data by using empirical laws, while LEO-PMW and -AMW sensors, which have better sensing through clouds, have a lower spatiotemporal resolution [16].

In this framework, various IR and PMW/AMW sensor-based products have been developed to estimate surface precipitation during the last decades. Additionally, products such as the "Hydro Estimator" (HE; [17]) or the "Precipitation Estimation from Remotely Sensed Information Using Artificial Neural Network" (PERSIANN; [18]), which are IR sensor-based products, can be associated with PMW/AMW sensor-based retrievals [1], such as the "Climate Prediction Center MORPHing" technique (CMORPH; [19]), the "Global Satellite Mapping of Precipitation" (GSMaP; [20]), or products provided by NASA under the Global Precipitation Measurement (GPM) programme, such as the "Integrated Multi-SatellitE Retrievals for GPM" (IMERG; [21]). More recently, an innovative technique has been developed to estimate precipitation using the quality and attenuation of signals' broadband communication satellites [22,23]. According to the satellites, and the sensors and assumptions used to develop the different rain products, performances in the precipitation estimates at global and/or at finer scales can be impacted.

The objective of this study is to evaluate the rain estimations of nine satellite products during two rainy events, with contrasted intensities, which occurred over France in 2022. For both cases, a comparative approach with rain gauges and ground-based radar measurements for cumulative rain amounts was used to evaluate each satellite product. This paper is organised as follows: after a description of the data, the methodology as well as the case studies are described in Sections 2 and 3 presents the results of the comparative analyses for rain amounts. Section 4 provides a discussion of the strengths and weakness of the products evaluated in this study, while Section 5 concludes and gives some perspectives.

2. Materials and Methods

2.1. Description of the Precipitation Products

The rainfall products used in this study are divided into 3 categories: from rain-gauge network, from ground radar network, and from satellite measurements. Each product has its own spatial, temporal, and accessibility features (Table 1).

Table 1. Description of the precipitation data used in this study. All products were freely accessed with the exception of RADOME, PANTHERE, and OPERA under license and DATABOURG being a commercial product.

Dataset	Type of Data	Spatial Coverage	Spatial Resolution	Temporal Resolution	Data Latency	Availability
RADOME	Rain gauges network	France	-	1 h	Real-time	https://donneespubliques.meteofrance.fr, accessed on 19 November 2023
PANTHERE	Radar network	France	1 km^2	15 min	Real-time	https://donneespubliques.meteofrance.fr, accessed on 19 November 2023
OPERA	Radar network	Europe	4 km^2	15 min	Real-time	https://portail-api.meteofrance.fr/web/fr/, accessed on 19 November 2023
IMERG-Early	Satellite	60° N–60° S	0.1° × 0.1°	30 min	4 h	https://disc.gsfc.nasa.gov/datasets/GPM_3IMERGHHE_06/summary, accessed on 19 November 2023
IMERG-Late	Satellite	60° N–60° S	0.1° × 0.1°	30 min	14 h	https://disc.gsfc.nasa.gov/datasets/GPM_3IMERGHHL_06/summary, accessed on 19 November 2023
CMORPH-RT	Satellite	60° N–60° S	0.08° × 0.08°	30 min	3 h	https://ftp.cpc.ncep.noaa.gov/precip/CMORPH_RT/, accessed on 19 November 2023
CMORPH	Satellite	60° N–60° S	0.08° × 0.08°	30 min	18 h	https://ftp.cpc.ncep.noaa.gov/precip/CMORPH_V0.x/, accessed on 19 November 2023
GSMaP-Now	Satellite	60° N–60° S	0.1° × 0.1°	30 min	Real-time	https://sharaku.eorc.jaxa.jp/GSMaP_NOW/, accessed on 19 November 2023
GSMaP-Now-GC	Satellite	60° N–60° S	0.1° × 0.1°	30 min	Real-time	https://sharaku.eorc.jaxa.jp/GSMaP_NOW/, accessed on 19 November 2023
GSMaP-NRT	Satellite	60° N–60° S	0.1° × 0.1°	1 h	4 h	https://sharaku.eorc.jaxa.jp/GSMaP/, accessed on 19 November 2023
GSMAP-NRT-GC	Satellite	60° N–60° S	0.1° × 0.1°	1 h	4 h	https://sharaku.eorc.jaxa.jp/GSMaP/, accessed on 19 November 2023
GHE	Satellite	60° N–60° S	0.04° × 0.04°	15 min	2 h	https://www.noaa.gov/nodd/datasets, accessed on 19 November 2023
PDIR	Satellite	60° N–60° S	0.04° × 0.04°	1 h	2 h	https://persiann.eng.uci.edu/CHRSdata/PDIRNow/netcdf_1h/, accessed on 19 November 2023
DATABOURG	Satellite	France	1 km^2	5 min	Real-time	https://databourg.com/, accessed on 19 November 2023

2.1.1. RADOME Rain Gauges Network

The in situ dataset used in this study comes from the “Réseau d’Acquisition de Données et d’Observation Météorologiques Etendues” (RADOME network; [24]) provided by Météo-France. This network covers mainland France and contains nearly 600 operational stations providing data in real time [25]. It constitutes tipping-bucket rain gauges with a precision of 0.1, 0.2, or 0.5 mm from one rain gauge to another, corresponding to the bucket capacity. The mean distance between two stations of the RADOME network is approximately 30 km. For our study, we use the RADOME dataset aggregated over 1 h provided by the company Weather-Measures.

2.1.2. Radar Networks

In this study, data from two radar networks were used: the Météo-France PANTHERE rain-rate composite product [26,27] and the OPERA pan-European composite product [28]. Both of these products are mainly based on observations from the national radar network when focussing on rainy events over France but some differences exist in data treatments or instruments, which can impact the rain estimates.

The ARAMIS French radar network [13] is composed of 31 Doppler radars that use various frequencies (or bands): 5 are in the S-band, 20 are in the C-band, and 6 are in the X-band [29] (see Figure 1). An additional C-band radar, operated by the company NOVIMET, is located at the Mont Vial summit (43.89° N, 7.15° E) in south eastern France, and two other radars, located at the Paris-Charles de Gaulle and Nice airports, contribute to the French PANTHERE product [30]. Moreover, two partner radars which do not take part in the ARAMIS network are used within the PANTHERE product (both are located on the Jersey Island and at the station La Dôle/Geneva at the France–Switzerland border).

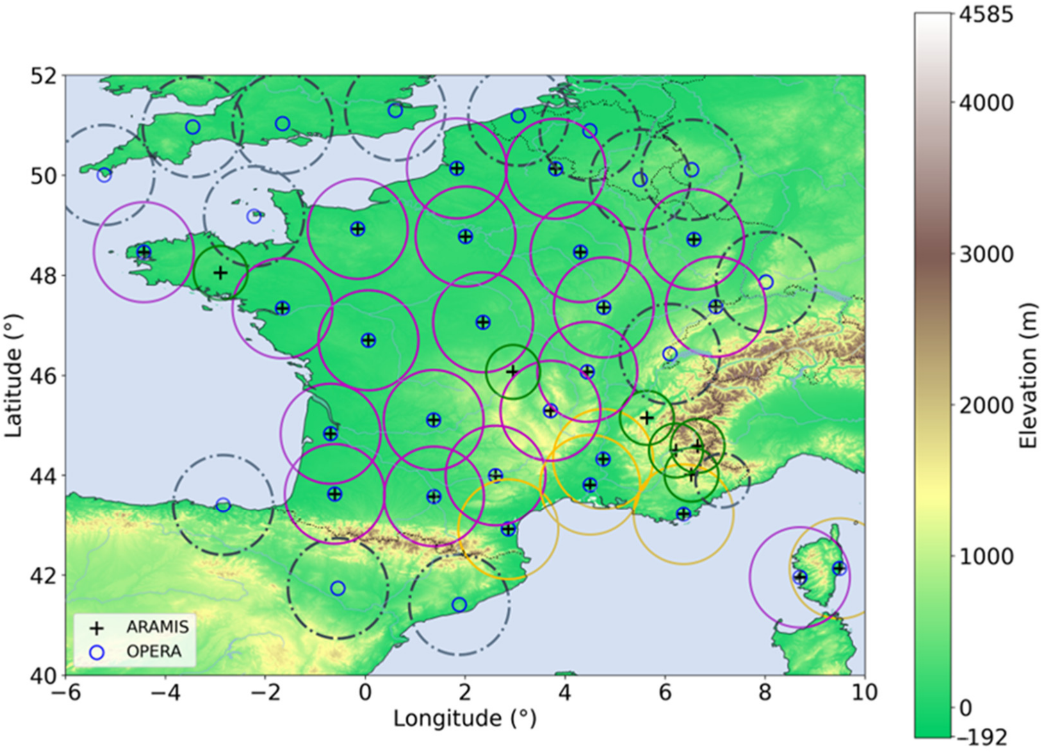

Figure 1. Positions of the radars of the ARAMIS network (plus symbols) considered in the PANTHERE product. Radars of the OPERA product are identified with small blue circles. Additional coloured circles are used to indicate the type of the radar and an extension of measurement: the C-band (magenta, 100 km), S-band (yellow, 100 km), and X-band (green, 60 km) radars. The C- and S-band radars are only considered in the OPERA product and those located close to the French borders are indicated with dashed-dotted black circles.

The data processing took into account polarimetric and reflectivity parameters sampled on a polar grid with a resolution of 240 m × 0.5° [29]. For the C- and S-band radars, a radius of 100 km around the radar position was considered for the measurement of precipitation amounts, whereas a range of about 200 km around the radar position was used for precipitation detection [31]. The X-band radars were used as gap-fillers [27]. The sampling volumes were produced every 5 min and were built from three to five scans at a low-elevation angle (ranging from 0° to 3°) repeated every 5 min and from two to three scans at high-elevation angles (from 3° to 15°) [29]. These raw scans were received and processed by the French national centre according to the different steps detailed in [26]. Figueras I Ventura and Tabary [27] provided a flow diagram that describes the different steps used in the data processing of the operational radar observations to obtain the rain-rate product:

- A ground-clutter identification by using pulse-to-pulse fluctuation of the radar reflectivity with further analysis for pixels adjacent to an identified clutter pixel;
- Non-meteorological echoes and precipitation-attenuation corrections from polarimetric modules;
- A partial beam-blockage correction by numerically simulating the interaction between the radar wave propagation and the ground by using orographic maps and long-term precipitation accumulation to identify trees and anthropogenic structures;
- A vertical profile of reflectivity correction deriving from ratios of hourly rainfall accumulation at different elevation angles and using these ratios to determine an optimal vertical profile reflectivity scheme from a predefined set;
- A gas-attenuation correction depending on the wavelength used and the altitude above the sea level;
- The synchronization or correction for advection;
- A weighted linear combination of the corrected reflectivity measurement at different elevation;
- The reflectivity (Z) conversion to rain rate (R) by using the Z-R relationship $Z = 200 \cdot R^{1.6}$, the 5 min rainfall accumulation;
- The rain-gauge adjustment.

In our case, we used the aggregated 15 min PANTHERE dataset provided by the company Weather-Measures.

The "European Operational Program for Exchange of weather RAdar information" (OPERA) was established in 1999 and constituted of 30 member states operating over 200 radars in the C-, X- and S-band [28]. The goal of this program is to organise a European cooperation of radar-products exchange with the help of the European national weather services and to build radar composites for the European Meteorological Network EUMETNET [14]. Hence, it is worth noting that the French ARAMIS radar network serves as a foundation of the radar coverage for OPERA over France, with the notable exceptions of the X-band radars that are not included; the locations are given in Figure 1. The processing and corrections made on the radar composites can be synthesised in 4 steps:

- An anomaly-removal module identifying non-weather-related pixels;
- A hit-accumulation clutter filter which detects pixels with an occurrence frequency higher than a reference threshold of 0.6;
- A beam-blockage correction;
- A satellite-based filter of residual non-rain echoes from the probability of the Precipitation Clouds product of the EUMETSAT Nowcasting Satellite Application Facilities.

The Z-R conversion is based on the same Marshall-Palmer relationship ($Z = 200 \cdot R^{1.6}$) as in the PANTHERE product. Park et al. [32] mentioned several points of improvement, such as follows:

- The differences between the radars in the network;
- The contamination by non-meteorological targets (partially corrected as explained earlier and in [28] with the implementation of a hit-accumulation clutter);
- The absence of correction of the vertical profile of reflectivity of the raw scans;
- The use of the single Marshall-Palmer relationship to convert Z to R.

Huuskonen et al. [14] indicated that 3 different OPERA products at 4 km^2 spatial resolution are available: the rain-rate composites with a 15 min timestep, the reflectivity composite with a 15 min timestep, and the hourly rainfall-accumulation composite. For this study, we use the rain-rate composite with a timestep of 15 min.

2.1.3. Satellite Precipitation Products

Low Earth Orbit (LEO) and geostationary (GEO) satellites can carry instruments providing precipitation amounts at the surface. Sun et al. [12] listed the three categories of sensors that measure the precipitation: the infrared or visible sensors aboard LEO and GEO satellites, the passive and active microwave (PMW/AMW) sensors aboard LEO sensors, and the blended products from the combination of both techniques. Another way to estimate the precipitation accumulation is based on the attenuation of Ka-band signals of broadband communication satellites [22,23].

IR Sensor-Based Satellite Products

To provide global rain-rate estimates, IR sensors are usually used onboard GEO satellites [1], which allow for a high temporal resolution (every 30 min or even less) [12]. The estimations of rain rates (R) are given by empirical relationships between R and the cloud-top brightness temperature T_b [15,33]. Being strongly related to the cloud heights, this type of estimation presents some limitations, such as a strong association to convective rain regimes, and conversely with non-convective rainfall, or the difficulty to distinguish precipitation patterns over complex terrain [34].

The Global Hydro Estimator (GHE) is derived from the Hydro-Estimator algorithm (HE; [17]), which is provided by the National Oceanic and Atmospheric Administration—National Environmental Satellite, Data and Information Service. GHE instantaneous rain-rate product has a spatial resolution of 4×4 km^2 and a temporal resolution of 15 min (see Table 1), and uses estimations of cloud-top brightness temperature from IR sensors. GHE uses a fixed relationship between these cloud-top brightness temperatures and rain rates, calibrated with radar data [35]. GHE includes the information given by the National Centres for Environmental Prediction Global Forecast System (GFS) model to complete its algorithm [36]. GHE inputs can use regional model outputs, such as those for South America [37]. Georgakakos et al. [38] also considered the eventuality of associating GHE skills and PMW sensors.

The Precipitation Estimation from Remotely Sensed Information Using Artificial Neural Network (PERSIANN) Dynamic Infrared Rain Rate (PDIR) was developed by the Centre for Hydrometeorology and Remote Sensing (CHRS) at the University of California [39]. Initially, the PERSIANN algorithm [18] was based on the artificial neural network technique to estimate rainfall accumulation. Then, the PERSIANN—Cloud Classification System (PCCS) resumed the same PERSIANN features; however, the PCCS classifies cloud-patch features based on the texture, geometry, dynamic evolution, and cloud-top height of clouds from IR sensor-based satellite estimates [40] and does not use PMW data unlike PERSIANN [33]. This cloud classification is performed by using a variable threshold cloud segmentation algorithm and varies the T_b-R relationships. The PDIR algorithm is a near-real-time (NRT) precipitation product like the PCCS, with several modifications developed by Nguyen et al. [33]:

- A better identification of warmer stratiform clouds from higher temperature thresholds;
- An improvement in the watershed method used for the image segmentation;
- An improvement in the rainfall regime identification by adding monthly sets of cloud types to the existing cloud classification system;
- The use of PMW satellite data to adjust T_b–R curves;
- The integration of climatology data from WorldClim version 2 [41] over land and PERSIANN Climate Data Record (PCDR; [42]) over the ocean to create a dynamical T_b–R curve model.

In this study, PDIR is an NRT precipitation product and provides 4 × 4 km^2 gridded rain-rate estimations with an hourly temporal resolution.

Microwave Sensor-Based and Blended Products

Two types of microwave-based sensing techniques were used in this study:

- PMW sensors measure the upwelling radiation from the Earth's surface which is affected by precipitation-sized particles [1]. This upwelling radiation is affected differently depending on the iced or liquid nature of the particles [43];
- AMW sensors are the most direct way to estimate precipitation amounts because they are based on the analysis of backscatter signals from rain-sized target particles [1,44], such as ground-based weather radars [45].

However, PMW and AMW sensors are carried by LEO sensors only [12]. Estimations with PMW and AMW sensors provide a "snap-shot" detection of precipitation fields below the satellite [46], leading to a coarser temporal sampling compared to GEO satellite IR imagery [12]. To counter this, these sensors need to be carried onboard a constellation of LEO satellites [44]; however, for now, microwave sensors onboard LEO satellites give global coverage every 3 h [12].

CMORPH (CPC MORPHing) is a multi-satellite-based and PMW-derived precipitation product developed by the Climate Prediction Centre (CPC) of the NOAA [19]. The CMORPH products used in this study have a 30 min temporal and 8 × 8 km^2 spatial resolutions. The CMORPH algorithm uses the estimates derived by PMW sensors, propagates the precipitation fields from the motion vectors determined from IR sensors observations, and uses a morphing technique which smooths the fusion of precipitation-pattern propagations backward and forward in time. Two products, derived from this algorithm, were used in this study:

- The CMORPH-RT [47], which propagates PMW sensor-based estimates only forward in time making them available in real time;
- CMORPH v0.x based on the morphing method [19].

The Global Satellite Mapping of Precipitation (GSMaP) is a project supported by the Japan Aerospace Agency (JAXA) (Tokyo, Japan) and the Japan Science and Technology Agency (Saitama, Japan) [20]. GSMaP rain-rate estimates were derived from PMW sensor measurements and the motion vectors were determined from successive IR images to propagate rain fields. Moreover, a refining step for the effects linked to the propagation was implemented by the use of a Kalman filter model [48]. Among all of the products presented in [49], four of them were retained with their associated gauge-calibrated versions: the near-real-time version 7 of GSMaP (GSMaP-NRT) based on the original GSMaP v7 algorithm and an instantaneous (GSMaP-Now) version of GSMaP with a half-hourly extrapolation, only forward in time, by using motion vectors determined by geostationary satellites [50]. Furthermore, as Ramadhan et al. [51] detailed, both GSMaP-NRT and GSMaP-Now products have gauge-adjusted versions (GSMaP-NRT-GC and GSMaP-Now-GC, respectively), which we used in this work, with the same latency and gauge-adjusting process. This process is detailed as follows [50]: the gauge measurement was not available in real-time, the gauge-adjusted versions were produced by adopting the error parameters derived from the gauge-corrected satellite precipitation product (GSMaP-Gauge) of the post-real-time product (GSMaP-MVK). Both GSMaP-Gauge and GSMaP-MVK were not used in this work because of their post-real-time latency of 3 days. The four products were given at a spatial resolution of $0.1° \times 0.1°$ (11 × 11 km^2). GSMaP-Now and GSMaP-Now-GC have a 30 min temporal resolution while the NRT version has an hourly timestep.

The space mission Global Precipitation Measurement (GPM) was launched in 2014 as part of a joint project between NASA and JAXA. In that framework, level 3 satellite precipitation products Integrated Multi-satellitE Retrievals for GPM (IMERG) were developed [21]. IMERG provides precipitation fields every 30 min, with a horizontal resolution of $0.1° \times 0.1°$ in latitude and longitude. These products emerge from a combination of data collected by IR and PMW sensors from the GPM constellation satellites. In this study, we used two different products from IMERG: IMERG-Early and IMERG-Late, which were both considered as NRT versions but with various post-processing procedures [52]:

- IMERG-Early (later called EARLY) is the earliest version of the IMERG product available after nominal observation; with approximately 4 h of data latency, the propagation of precipitation fields determined by the observation of IR sensors is applied only forward in time;
- IMERG-Late version (later called LATE) is available after a latency of 14 h and has its precipitation fields propagated forward and backward in time.

Version 6 of the IMERG products was used for this study. All the details about the different MW products used in this study are given in Table 1.

Carrier-to-Noise-Based Precipitation Product

DATABOURG is a commercial product provided by the Databourg Systems Company based in Luxembourg. This product is based on broadband satellite Ka-band signals [22,23]. Broadband satellite systems provide bidirectional communications between gateway stations and terminal users, allowing for internet provisioning [22]. The forward and return signals are monitored by the gateway, and a carrier-to-Noise (C/N) parameter is computed by measuring the quality of the communication link and received signal [22]. The C/N measurement was used in an artificial neural network technique to obtain a rain-regime classification required to determine a reference condition and the signal attenuation [53]. Finally, the rain rate was empirically deduced from the attenuation, with Ka-band signals being heavily attenuated in strong-intensity rain and less in light-rain conditions [53,54]. In this study, we used the 5 min temporal resolution final product interpolated on a 1 km^2 grid.

2.2. Point-to-Pixel Comparative Method

Several different methods can be used to compare precipitation products on different spatial grids. Generally, point data such as that supplied by rain-gauge networks are interpolated on a defined grid according to different methods which can be divided into two categories [55]:

- Deterministic methods (e.g., the inverse distance weighting or the Thiessen polygons; [56,57]);
- Geostatistical methods (e.g., the different Kriging methods; [58]).

The choice of the selected interpolation mainly depends on factors such as the complexity of the topography or the density of the rain-gauge network [59].

In this study, we consider the original spatial resolution of the RADOME network as a reference. Hence, we compare the observed punctual rain-gauge values to their respective nearest estimated pixel by using the widely used point-to-pixel approach [8,59–62]. Moreover, the comparisons between the rain-gauge data and the diverse rain products were performed on the accumulated rain values obtained at the end of both case studies presented in Section 2.3. For each point–pixel considered (i), an absolute bias was calculated according to: $BIAS_i = E_i - O_i$ where O was the rain-gauge observations from the RADOME network while E was the estimations given by each precipitation product (i.e., radar or satellites) used in this study. Thus, a positive or negative bias corresponds, respectively, to an overestimation or an underestimation of the used precipitation product compared to rain-gauge observations.

2.3. Synoptic Description of the Two Case Studies

The two case studies observed over France in 2022 present different precipitation features. The April case (22–25 April 2022) which lasted 72 h produced precipitation over a large part of the south of France, whereas the June case (24–28 June 2022) lasted 96 h over the centre of France (Figure 2).

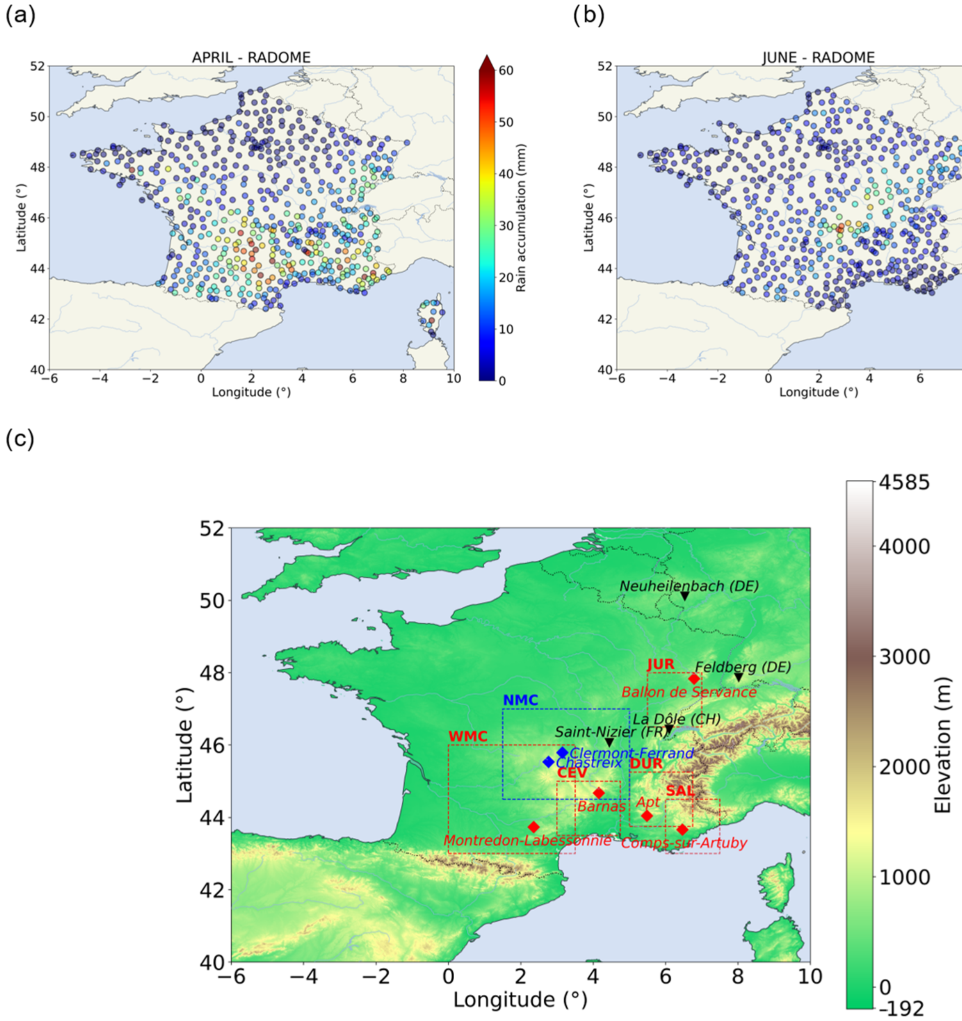

Figure 2. Rain accumulation measured by the RADOME rain-gauge network at the end of the April (**a**) and June cases (**b**). Panel (**c**) indicates localisations of the several areas of interest mentioned in the text. The red areas correspond to the April event, the blue areas correspond to the June event, and black markers are the localization of the radars mentioned in this study.

Figure 2a shows that the precipitations of the April case were mainly important over the mountainous areas, such as over the west of the Massif Central (WMC), South Alps (SAL), Durance valley (DUR), Cévennes (CEV), and Jura (JUR) (see Figure 2c for localisation) where the highest accumulations, respectively, observed were 75.9 mm at Montredon-Labessonnié (43.72° N, 2.33° E), 59.5 mm at Comps-sur-Artuby (43.66° N, 6.47° E), 62.4 mm at Apt (43.88° N, 5.40° E), 85.1 mm at Barnas (44.67° N, 4.17° E), and 31.8 mm at Ballon de Servance (47.83° N, 6.79° E). The median accumulated precipitations recorded over the mentioned regions were 26.6 mm, 31.4 mm, 23.5 mm, 22.3 mm, and 25.4 mm over WMC, SAL, DUR, CEV, and JUR, respectively.

For the June case, the precipitation amounts reached higher values around the northern Massif Central (NMC), such as at Chastreix (45.51° N, 2.74° E) and Clermont-Ferrand (45.79° N, 3.15° E) stations where 136.7 mm and 106.7 mm of rain were observed, respectively (Figure 2b). Nevertheless, the median accumulated precipitation recorded over this area was 35.7 mm.

The contrasted precipitation distributions observed for these two cases present different synoptic conditions displayed by the ECMWF ERA5 meteorological fields (Figure 3, [63]).

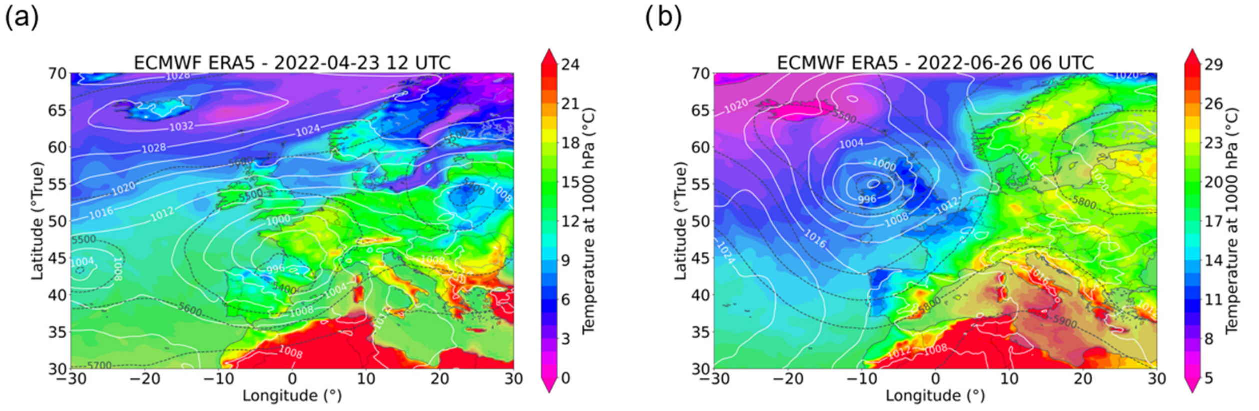

Figure 3. ECMWF ERA5 synoptic conditions on the 23 April 2022 at 12:00 UTC (**a**) and the 26 June 2022 at 06:00 UTC; (**b**) the temperature at 1000 hPa (in colours), the mean sea-level pressure (hPa) (white solid lines), and the 500 hPa geopotential (in $m^2 s^{-2}$, dashed grey lines).

For the April case, a marked depression located over northwestern Spain on 22 April slowly moved northeasterly with decreasing intensity. On 23 April 12:00 UTC, this depression was centred over southwestern of France (Figure 3a). Then, it disappeared, inducing a weak west–east stationary front in the middle of France.

For the June case, the temperature over France was warmer than for the April case. An intense depression was present over the British Isles and a weak anticyclone was over Italy (Figure 3b). These pressure systems were, respectively, associated with cold and warm temperatures inducing the formation of an intense cold front through France (Figure 3b). During the June case, the depression moved southeasterly, brought colder and more humid air mass over France. Thus, the more marked depression encountered during the June case brought intense precipitation along the cold front, whereas the less marked situation observed during the April case brought less-intense precipitation over a larger area (Figure 2).

3. Comparative Analyses Results

3.1. Rain-Gauge vs. Radar Observations

In this section, we compare the rain-gauge observations obtained from the RADOME network to the precipitation amounts estimated via radar observations obtained from either the PANTHERE network or the OPERA network (see Sections 2.1.1 and 2.1.2 for the description of the RADOME, PANTHERE, and OPERA networks) for both the April and the June cases.

3.1.1. PANTHERE vs. RADOME

For the April case (Figure 4a), precipitations were mainly located over the south of France, especially over the mountainous areas, as observed by RADOME (Figure 2a). Table 2 presents the rain maximum recorded by the radar and all other rain products used in this study, for each area of interest defined in Figure 2c, as well as the distance between each of these maxima and their RADOME counterpart.

Table 2 indicates that PANTHERE recorded a rain maximum of 98.1 mm, 89.0 mm, 69.5 mm, 72.1 mm, and 44.1 mm over the WMC, SAL, DUR, CEVs and JUR areas, respectively. Except over CEV, PANTHERE recorded higher maxima precipitation accumulations than RADOME. The distance between RADOME and PANTHERE maximums was 32.29 km in SAL, 10.41 km over CEV, and 14.18 km over JUR. However, the distance increased to 225.54 km over WMC and to 107.99 km over DUR. Regarding the median precipitation accumulations estimated by PANTHERE (given by Table 3) over the same areas, they were equal to 24.8 mm over WMC, 30.5 mm over SAL, 28.0 mm over DUR, 30.1 mm over CEV, and 25.4 mm over JUR. These values were close to the values observed by RADOME: 26.6 mm for WMC, 31.4 mm for SAL, 23.5 mm for DUR, 22.3 mm for CEV, and 22.6 mm for JUR. Nevertheless, we can notice a trend of overestimating the accumulation in the CEV and SAL regions. Near the Mediterranean coasts, RADOME measured an amount less than 20 mm of precipitation where PANTHERE estimated up to 30 mm of precipitation accumulation.

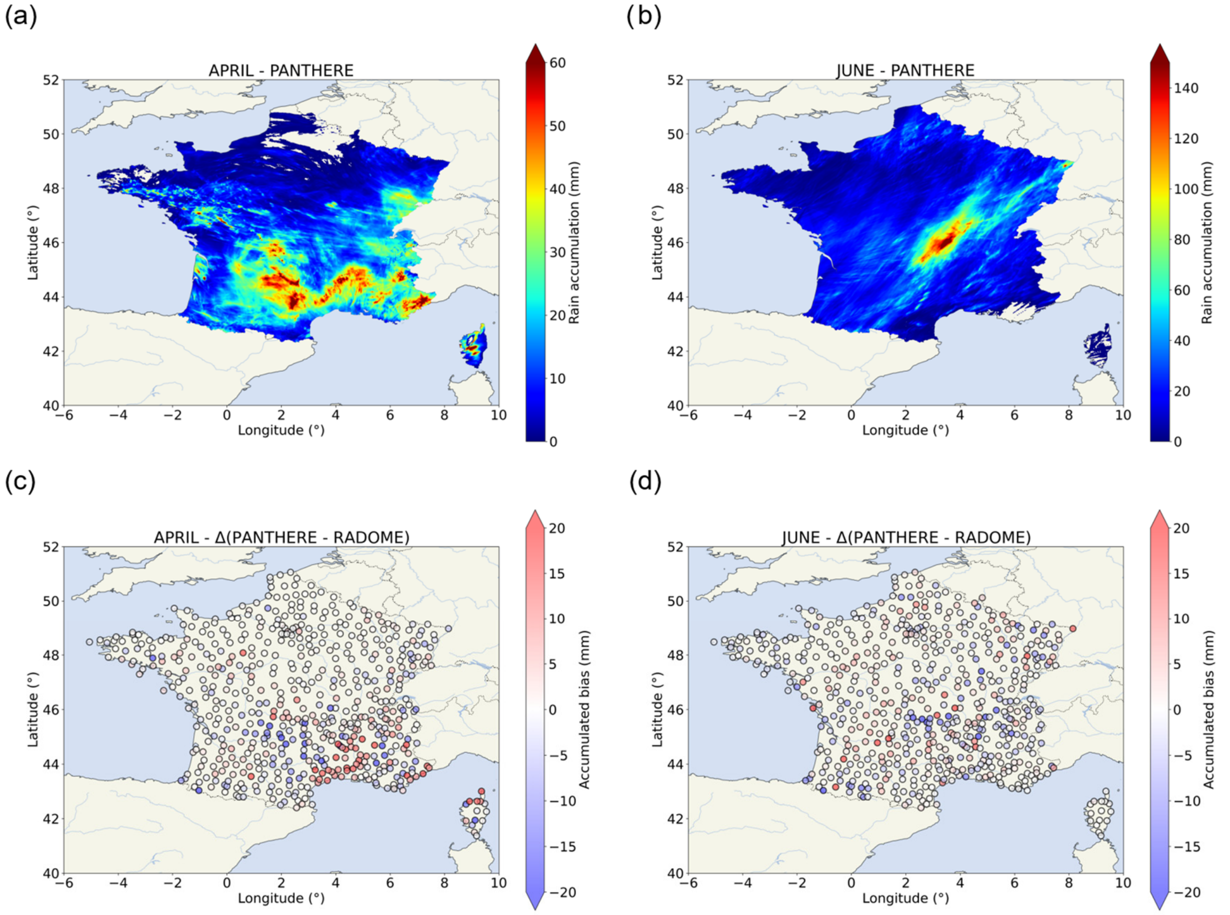

Figure 4. Precipitation accumulation estimated by PANTHERE from the observations of the ARAMIS radars network at the end of (**a**) the April case and (**b**) the June case. Absolute biases with the RADOME precipitation gauges network using the point-to-pixel approach are also represented for both (**c**) the April case and (**d**) June case.

Figure 4c presents the absolute bias calculated comparing PANTHERE and RADOME at each RADOME station (using the method described in Section 2.2) for the April event. This comparison shows that PANTHERE underestimated the rain amounts in the south of the CEV area while it overestimated them in the WMC. We can observe that the main differences between PANTHERE and RADOME were localized over the mountainous areas, especially over the Massif Central, the Cévennes, and the Southern Alps. Table 3 gives the mean absolute bias calculated for each area of interest. PANTHERE had quite similar values compared to the rain gauges because the mean difference was lower than 2.14 mm. There was only one exception for the CEV region, where the mean absolute bias reached +6.89 mm.

Table 2. Maximum values (in mm) and the distance separating these maxima to their RADOME counterparts (in km) for the April and June cases. These values were determined considering the different stations inside the delimitated areas shown in Figure 2c: WMC for the western Massif Central, SAL for the south of the Alps, DUR for Durance, CEV for Cévennes, JUR for Jura, and NMC for the northern Massif Central.

Dataset	**April**										**June**	
	WMC		**SAL**		**DUR**		**CEV**		**JUR**		**NMC**	
	Max	**Dist.**	**Max**	**Dist.**	**Max**	**Dist.**	**Max**	**Dist.**	**Max**	**Dist.**	**Max**	**Dist.**
RADOME	75.90	-	59.50	-	62.50	-	85.10	-	31.80	-	136.70	-
PANTHERE	98.10	225.54	89.00	32.29	69.50	107.99	72.10	10.41	44.10	14.18	204.60	74.64
OPERA	131.85	182.19	82.56	26.32	76.07	53.48	199.62	26.46	63.41	22.42	293.23	71.81
PDIR	62.42	239.07	39.24	73.20	41.12	111.73	28.17	32.47	31.33	15.07	76.60	9.64
GHE	70.45	119.27	168.26	75.51	208.32	18.94	72.12	30.39	54.72	41.78	83.68	9.44
EARLY	96.69	11.88	34.24	37.23	101.47	147.30	63.53	129.90	124.63	53.64	223.86	69.93
LATE	91.03	17.79	40.17	37.23	110.97	147.30	54.42	93.59	116.43	53.64	211.99	69.93
GSMaP-Now	72.24	161.98	43.98	83.90	50.79	167.46	38.41	80.11	45.57	153.07	82.83	126.89
GSMaP-Now-GC	56.57	161.98	30.99	83.90	38.09	167.46	29.44	80.11	39.87	153.07	82.43	126.89
GSMaP-NRT	50.64	132.31	85.73	70.57	85.73	57.61	37.40	107.70	44.60	103.73	83.97	77.85
GSMAP-NRT-GC	62.71	132.31	84.53	70.57	84.53	57.61	43.17	107.70	59.99	103.73	51.15	77.85
CMORPH-RT	62.13	181.98	36.36	48.17	52.10	138.10	26.42	90.76	66.97	43.55	61.77	46.20
CMORPH	49.60	23.72	31.00	33.18	29.70	28.22	27.00	90.76	37.70	51.76	129.20	83.22
DATABOURG	43.62	6.68	39.49	34.89	30.46	16.07	51.70	15.18	27.17	108.96	133.23	157.18

Table 3. Median accumulated precipitation and the mean absolute biases (mm) for the April and June cases. The values were calculated using the point for the points inside the areas shown in Figure 2c: WMC for the western Massif Central, S. AL for the south of the Alps, DUR for Durance, CEV for Cévennes, JUR for Jura, and NMC for the northern Massif Central.

Dataset	**April**										**June**	
	WMC		**SAL**		**DUR**		**CEV**		**JUR**		**NMC**	
	Median	**Mean Bias**	**Median**	**Mean Bias**	**Median**	**Mean Bias**	**Median**	**Mean Bias**	**Median**	**Mean Bias**	**Median**	**Mean Bias**
RADOME	26.60	-	31.40	-	23.50	-	22.30	-	25.40	-	35.70	-
PANTHERE	24.80	−2.14	30.50	+1.95	28.00	+0.05	30.10	+6.89	22.60	−0.57	35.00	−0.73
OPERA	29.14	+1.09	22.26	−3.70	16.11	−9.13	29.11	+5.15	27.63	+6.51	50.03	+14.13
PDIR	10.35	−16.17	9.63	−22.26	16.06	−9.70	7.22	−17.77	15.21	−8.73	24.79	−18.02
GHE	30.10	+1.25	50.46	+12.22	41.88	+17.07	32.53	+5.42	36.10	+11.29	33.44	−12.86
EARLY	29.97	+0.47	13.01	−15.51	15.58	−7.87	17.71	−4.33	40.85	+20.87	28.42	−4.55
LATE	30.41	+0.89	13.39	−14.99	15.65	−7.82	19.96	−3.63	41.69	+24.69	32.25	−0.58
GSMaP-Now	23.00	−3.69	9.19	−21.05	14.61	−10.68	12.04	−11.99	18.65	−4.78	19.77	−19.63
GSMaP-Now-GC	17.96	−8.95	5.98	−24.44	10.53	−15.05	8.91	−15.42	18.05	−5.54	19.43	−20.57
GSMaP-NRT	16.68	−12.22	21.12	−14.06	16.61	−10.64	16.74	−8.67	19.27	−3.72	26.02	−15.73
GSMAP-NRT-GC	20.42	−8.47	19.57	−15.46	17.49	−10.39	18.69	−6.51	26.09	+3.84	15.85	−26.17
CMORPH-RT	19.19	−8.34	12.53	−14.99	16.23	−7.53	14.61	−10.83	27.17	+12.84	20.78	−19.26
CMORPH	20.90	−8.20	11.50	−16.78	12.90	−14.53	14.80	−11.43	23.50	−0.91	37.90	+1.25
DATABOURG	21.68	−6.83	27.05	−4.35	22.25	−6.59	20.14	−3.11	18.47	−5.54	49.86	+8.94

For the June event, PANTHERE detected a localized high-intensity precipitation pattern over the north of the Massif Central (NMC area) extended on a southwest–northeast axis (Figure 4b), as RADOME. The maximum of precipitation accumulation estimated by PANTHERE over NMC was 204.60 mm and was located 74.64 km away from the rain maximum captured by RADOME (Table 2). However, the median of the rain accumulation for the NMC area (35.0 mm) was close to the RADOME one (35.7 mm) for this event. We can see that the main differences in the rain distribution between RADOME and PANTHERE were, as for the April case, located over the reliefs of the Massif Central area (Figure 4d). The mean bias computed for the NMC area was equal to −0.73 mm (Table 3) and an underestimation of −29 mm was recorded at the Chastreix RADOME station.

3.1.2. OPERA vs. RADOME

Figure 5 shows the precipitation accumulation estimated by the OPERA product for the April and June cases, and absolute biases in precipitation accumulations between OPERA and RADOME at each rain-gauge station.

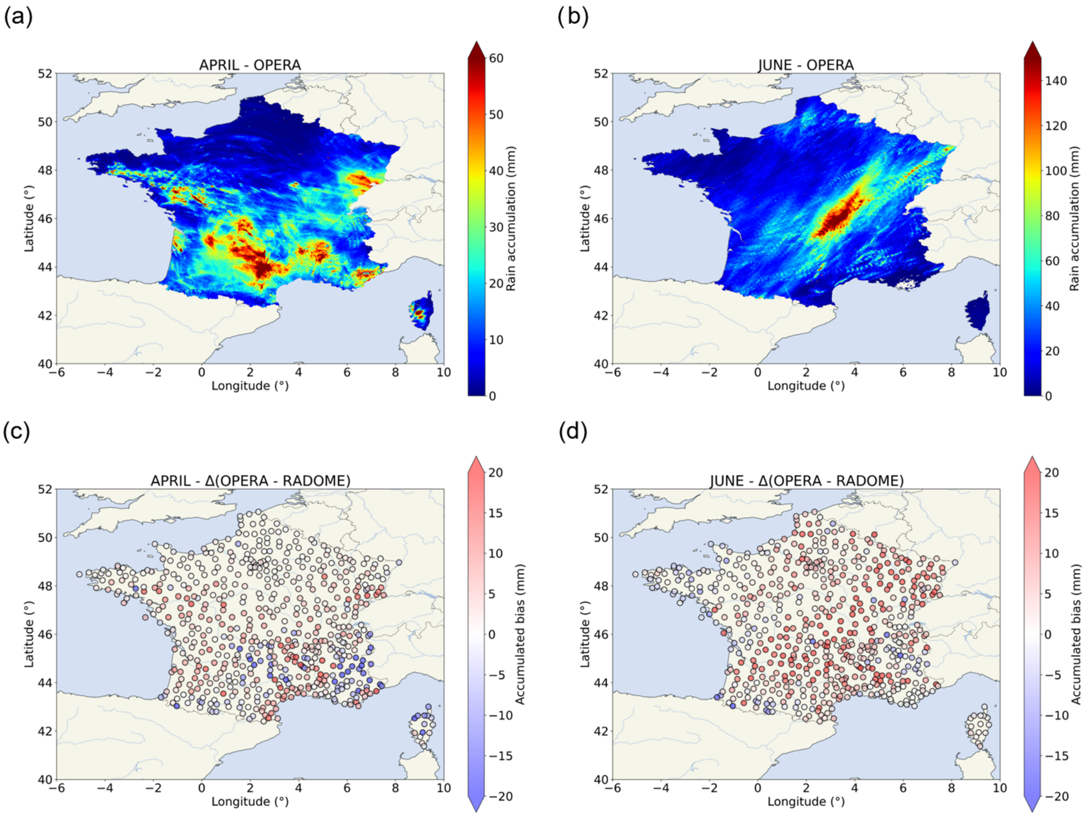

Figure 5. As in Figure 4, but for the OPERA product.

For the April case (Figure 5a), as in the RADOME observations, the precipitations obtained with OPERA were mainly situated over the mountainous areas of the south of France but the extension of the intense precipitation was more important than in RADOME (Figure 2a), especially in the WMC area (Figure 2c). Table 2 shows that the maxima of rain obtained for the different areas of interest with OPERA were higher than RADOME (131.85 mm for WMC, 82.56 mm over SAL, 76.07 mm over the DUR, 199.62 mm over CEV, and 63.41 mm over JUR). The positions of these maxima were less than 53.48 km from the maximum values measured with the RADOME rain gauges for all the areas of interest, except for the WMC area where the OPERA maximum was at 182.19 km (Table 2). Regarding the median values obtained with OPERA for the precipitation accumulation, they were higher than the RADOME ones for WMC, CEV, and JUR, whereas they were lower for SAL and DUR. These trends are also shown in Figure 5c, since an intense underestimation and overestimation are visible, respectively, over the DUR and the JUR areas, especially near the France–Germany border for the latter. Table 3 shows that the mean absolute biases reach −9.13 mm for DUR, −3.70 mm for SAL, +6.51 mm for JUR, and +5.15 mm for CEV. However, the mean absolute bias is only +1.09 mm for WMC.

For the June case, the precipitation event was localised on the same southwest–northeast axis (Figure 5b) as in the RADOME observations (Figure 2b). However, the area wetted by intense rain amounts (greater than 100 mm) is more extended than in the RADOME observations. The maximum rain amount estimated by OPERA was equal to 293.23 mm over the NMC area (Table 2), which is two times higher than that observed using rain gauges. Moreover, this maximum value was located at a distance of 71.81 km from the RADOME one (Table 2). Figure 5d shows that the rain amounts were generally overestimated by OPERA. Only a few stations randomly sparse over France presented weak underestimations of rain amount in OPERA, as near the France–Spain border or over the northern Alps. The bias at the Chastreix station was +14.7 mm and the average bias of +14.13 mm recorded over the NMC area (Table 3) confirms the global overestimation trend.

3.1.3. PANTHERE and OPERA vs. RADOME

Over France, the rain amounts provided by both PANTHERE and OPERA radar products were based on a quasi-identical radar network. These differences between the two radar products could reside in the processing applied by Météo-France, for PANTHERE, and by EUMETNET, for OPERA. The rain accumulated patterns were quite similar in PANTHERE (Figure 4a,b) and OPERA (Figure 5a,b) for both cases, but there were few differences locally.

In order to better quantify the differences in the rain estimates from both radar products compared to the rain-gauge observations, Figure 6 presents the absolute biases obtained using OPERA compared to those obtained using PANTHERE as a function of the RADOME values for both cases (without distinguishing the areas defined in Figure 2c).

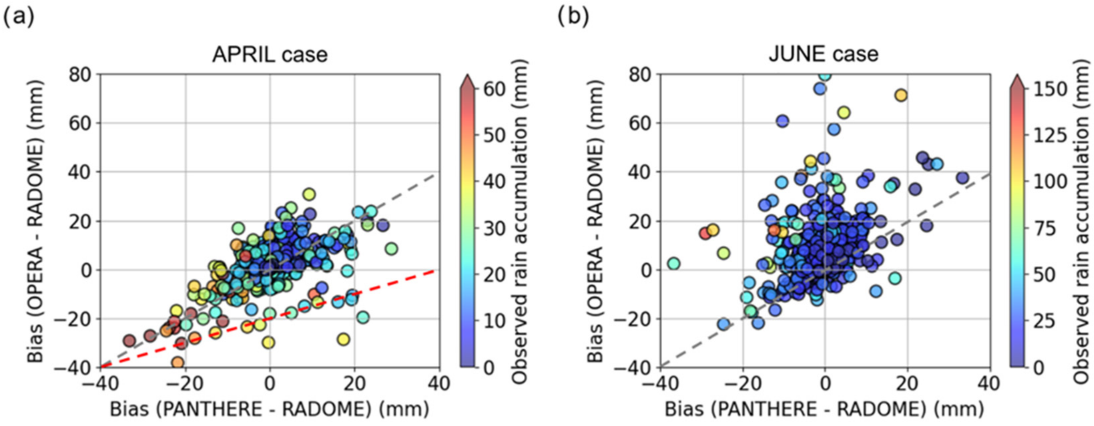

Figure 6. Comparison of the biases obtained between both radar products (OPERA and PANTHERE) and the RADOME rain-gauge network. Colours correspond to the accumulated precipitation values observed by the RADOME rain gauges for both (**a**) the April and (**b**) the June cases. The grey dashed line represents the 1:1 curve. The red dashed line corresponds to a specific situation defined in the text.

Figure 6 shows that OPERA provided generally higher rain amounts than PANTHERE for both cases. For the April case, both radar products tended to agree with the RADOME observations when rain gauges captured rain amounts up to 20 mm but the main differences appeared when rain gauges captured rain amounts higher than 40 mm. In that case, both radar products greatly underestimated (by more than −20 mm) the rain amounts. We can also note that the observations of a few rain-gauge stations seem greatly underestimated by OPERA, while PANTHERE provided rain values less underestimated or slightly overestimated (dashed red line in Figure 6a). For the June case, Figure 6b shows that the absolute biases were between −20 mm and +20 mm with PANTHERE, whereas they were between −20 mm and +40 mm with OPERA (compared with RADOME observations).

Moreover, Figures 4a,b and 5a,b, show that even though both radar products well-detected the presence of precipitation over the reliefs of the south of France or over the north of the Massif Central for the April or the June case, respectively (as in RADOME, Figure 2a), a few major differences could be observed. Indeed, for the April case, the zone where the rain accumulation was greater than 55 mm was more extended in OPERA (Figure 5a) than in PANTHERE (Figure 4a), and OPERA recorded light precipitation accumulations (<3 mm) in the north of France, whereas a larger no-precipitation zone was observed by PANTHERE. For the June case, Figure 5b shows that the zone where the rain amounts were greater than 100 mm was more extended in OPERA than in PANTHERE, explaining that the important difference in the mean absolute bias calculated over the NMC was with the two radar products (Table 3). Note that the field of the high accumulated rain amounts at the surface seemed more discontinued in OPERA than in PANTHERE (e.g., over the northeast of France in Figure 5b compared to Figure 4b), which was due to the different spatial resolutions of the two radar products (see Table 1).

Focussing on the specific areas defined in Figure 2c for the April case, OPERA maximum estimates were higher than the PANTHERE ones for the WMC, DUR, CEV, and JUR (Table 2). We can also note that even if the mean absolute biases were quite comparable for WMC, SAL, and CEV in the PANTHERE and OPERA products, the trends were opposite for two of them (Table 3). Moreover, the differences in the rain amounts estimated by both radar products became more striking for DUR and JUR (see Table 3). Indeed, for these specific areas, the median of the accumulated rain amounts was equal to 28.0 mm in PANTHERE and 16.11 mm in OPERA for DUR, while it was equal to 22.6 mm in PANTHERE and 27.63 mm in OPERA for JUR. Figures 4a and 5a also show that the rain distributions were quite different over these two specific areas for the April case.

In order to explain the main differences obtained in PANTHERE and OPERA over the DUR and JUR areas for the April case, we compared the spatiotemporal evolution of the precipitation fields, focussing on the zones watered by more than 2 mm of rain over a 3 h period. Figures 7 and 8 present the results for the DUR (and SAL) and the JUR areas, respectively.

Figure 7a–d shows that PANTHERE estimated important rain amounts over the Alps (DUR area) during all of the 23 April 2022 in accordance with the RADOME rain gauges, whereas the rain estimated with the OPERA radar product were insignificant. This difference between the two radar products explains most of the diverging values between OPERA and PANTHERE presented in Figure 6a (see the red dashed line). Figure 7 also presents the range of the different radars which were used either in the PANTHERE product or in the OPERA product (also presented in Figure 1). Thus, over this specific area, PANTHERE was constructed using the observations performed by several X-band radars located in the Alps, whereas OPERA was not [28], leading to a loss of radar spatial coverage and, therefore, a loss of the precipitation visibility over this region.

Over the JUR area, PANTHERE and OPERA presented different rain features for a period of approximately 6 h on 24 April 2022 (Figure 8), causing an important overestimation of the OPERA rain amounts (Table 3). As previously discussed for the DUR area, this difference could also be due to the number and position of the radars used in the different products. Indeed, in that case, two additional radars located close to the French–German–Swiss border were considered in the OPERA product (Figure 1): the Feldberg radar in southwestern Germany (47.87° N, 8.00° E) and the La Dôle radar in Switzerland (46.43° N, 6.10° E), which could influence the amounts of rain retrieved by the radar product over this area.

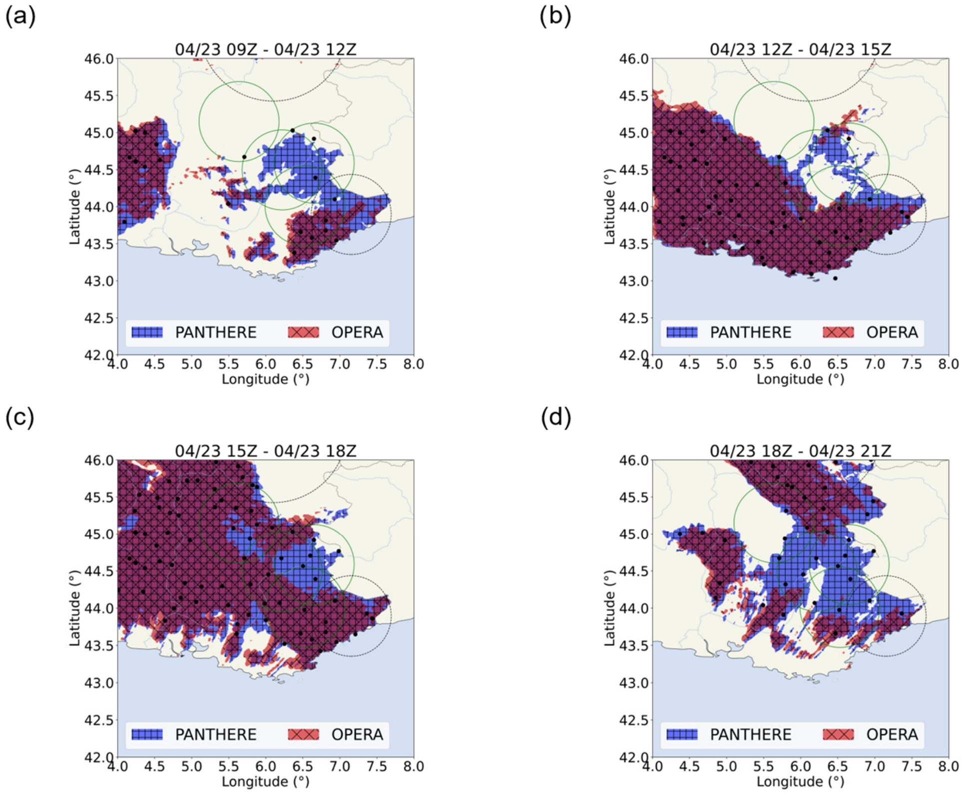

Figure 7. Temporal evolution of precipitation over DUR and SAL areas having more than 2 mm over a 3 h period according to PANTHERE (blue) and OPERA (red) on 23 April 2022 from 9 to 12 UTC (**a**), 12 to 15 UTC (**b**), 15 to 18 UTC (**c**) and 18 to 21 UTC (**d**). The circles present the range of the radars which were used either in PANTHERE (green circles) or in OPERA (black dotted circles) (see Figure 1 also). The small filled black circle symbols represent the position of the rain gauges of the RADOME network that also recorded more than 2 mm of rain over the same 3 h period.

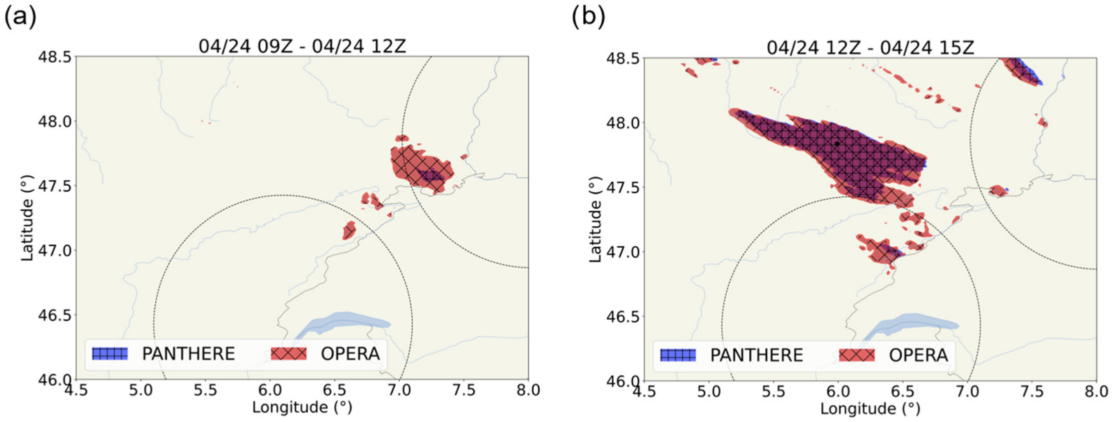

Figure 8. Temporal evolution of precipitation over JUR area having more than 2 mm over a 3 h period according to PANTHERE (blue) and OPERA (red) on 24 April 2022 from 9 to 12 UTC (**a**), and 12 to 15 UTC (**b**). The circles present the range of the radars which were used in OPERA (black dotted circles). The small filled black circle symbols represent the position of the rain gauges of the RADOME network that also recorded more than 2 mm of rain over the same 3 h period.

3.2. Rain-Gauge vs. Satellite Precipitation Products

In this section, we use the same methodology to compare the properties of rain amounts given by the satellite products and RADOME rain-gauge observations. The satellite precipitation products were divided into three categories: IR sensor-based products, MW sensor-based products, and C/R-based products.

3.2.1. IR Sensor-Based Product

Two IR sensor-based satellite precipitation products were used in this study: PDIR and GHE (see Section IR Sensor-Based Satellite Products). Figures 9 and 10 present the spatial distribution of the accumulated rain amounts for both cases, estimated using PDIR and GHE, respectively, as well as the results from the comparative analyses with the rain-gauge observations (using the point–pixel method described in Section 2.2).

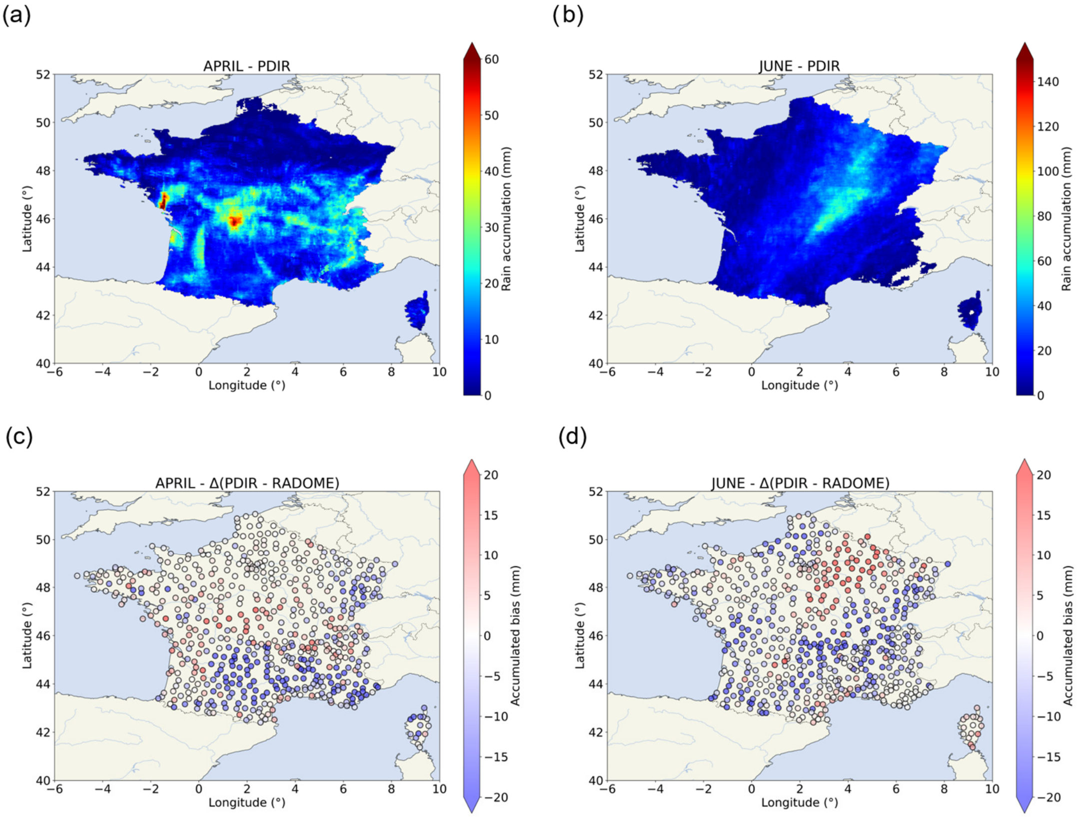

Figure 9. As in Figure 4, but for the PDIR product.

For the April case, Figure 9a shows that the PDIR product had difficulties locating the most intense rain amounts for the WMC area (i.e., more north than in the RADOME observations) and estimating the rain amounts over the south of France, especially for the CEV and SAL areas. For the June event (Figure 9b), the location of the watered area was better represented. However, the rain amounts retrieved by the PDIR product were seriously underestimated in that case. This was confirmed by the rain amounts given in Table 2: the maxima of the accumulated rain amounts were lower than observed by the rain gauges (by approx. 30% for the specific area defined over the south of France (Figure 2c) for the April case and by approx. 44% for the June case). Moreover, Table 2 reveals the important spatial error in the PDIR product because, for almost all the specific area, the rain maxima were located far from (up to 239.07 km for WMC) their RADOME counterparts. Figure 9c,d and Table 3 confirm the general underestimation of the rain amounts by the PDIR product, since the absolute biases for both cases were negative locally and on average.

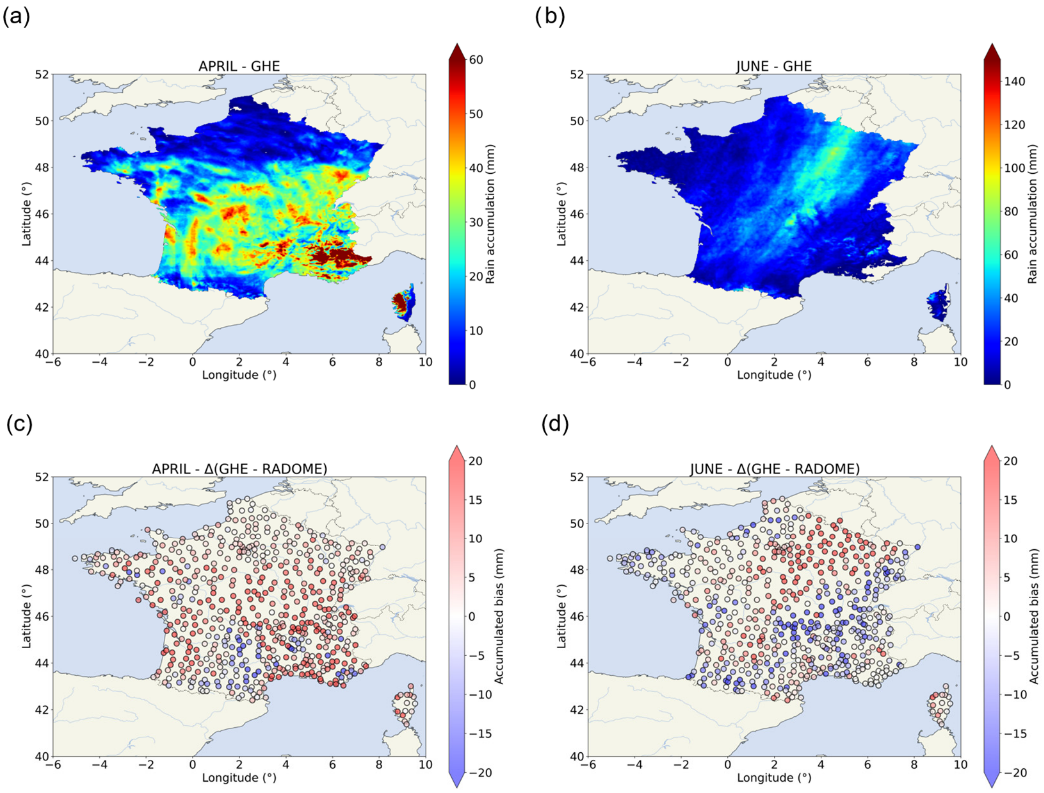

Figure 10. As in Figure 4, but for the GHE product.

Nevertheless, for the June event we can note that the PDIR rain amounts were slightly overestimated over the northeast part of France (Figure 9d), which could reveal a too-northerly trajectory of the precipitating system in PDIR. A strong underestimation was observed by comparing the PDIR estimations to RADOME observations (Table 3).

Figure 10a shows the representation of the precipitation amounts estimated by GHE during the April case. GHE tends to over-represent moderate to strong precipitation patterns and these strong intensity watered areas were more extended to the north than what RADOME observed. The highest precipitation amounts were observed over the southeast of the country and especially over the southern parts of the Alps. Table 2 reveals that all the estimated GHE maximums were larger than their RADOME counterparts over the eastern parts of the country. For the south and southwest areas, the GHE maximums tended to slightly underestimate the RADOME maximums (70.45 mm and 72.12 mm for GHE vs. 75.9 mm and 85.1 mm for RADOME over the WMC and CEV areas, respectively). However, the distance between the observed and estimated maximums was close to 100 km for the SAL, DUR, CEV, and JU areas, revealing that the GHE maximums tended to be slightly shifted from the RADOME maximums. For every area of interest, the GHE median values were greater than the RADOME ones (Table 3). This indicates that the moderate-intensity precipitation patterns were more frequent with GHE than with RADOME. The spatial bias distribution (Figure 10c) shows that GHE tended to overestimate the precipitation amounts observed over the Mediterranean littoral and to the north of the southern areas of interest (DUR, CEV, and WMC). Small areas of underestimation were observed in the east and southern parts of the WMC area, where the RADOME maximum was observed, but the trend shows a clear overestimation over every area of interest as seen in Table 3.

As for the June event (in Figure 10b), GHE estimated moderate-intensity precipitation amounts from the NMC area to the French–Belgium border. The GHE moderate-intensity estimations were more extended to the north than the RADOME observations, as seen with the April case. However, we did not see high precipitation estimations with GHE over NMC, unlike RADOME; for example, in Table 2 where GHE maximum was 83.68 mm against 136.7 mm for RADOME. These two maximums were located at a distance of 9.44 km, revealing that GHE tends to better localise the maximum during the June case than the April case. The bias distribution reveals that the overestimation signal was present more to the north of the observed location of the June case, while the position where the event took place was underestimated by the RADOME estimations. This point is confirmed when we look at the median of GHE estimations, which was 7 mm smaller than the median observed over the NMC area and the mean bias of −12.86 mm over the area.

We can see that PDIR had difficulty in to correctly identifying the precipitation patterns during the April case and for GHE to quantify the precipitation patterns over the east parts of the country. In general, the satellite-based precipitation estimations differed from the reference data (as in [64]) in low-intensity rainfall events (such as for our April case). Note that the majority of the studies which have used PDIR have been conducted over mountainous areas in lower latitudes, such as in California [64], Taïwan [65], Morocco [66], or Turkey [67], compared to the higher latitudes of France. One hypothesis that partially explains the north shift of both case studies' estimations is the parallax effect. This effect is caused by satellites with a high distance from the nadir, thus leading them to affect the clouds located in higher latitudes from the nadir more, such as the case in observed over Poland by using the Meteosat dataset [68]. The Meteosat dataset is included in PDIR and GHE algorithms as one of the GEO satellites inputs. For GHE, the algorithm might have observed the cold clouds present over France during the April event, which could explain the overestimation over the region.

3.2.2. MW Sensor-Based Product

In this section, an analysis similar to Section 3.2.1 is performed, focussing on accumulated rain amounts estimated via the MW sensor-based products described in Section Microwave Sensor-Based and Blended Products. To achieve this, we differentiated the used MW sensor-based products into three categories: the IMERG products (EARLY and LATE), the CMORPH products (default and -RT), and the GSMaP products (-Now and -NRT, either calibrated or not by rain gauges). Note that the Supplementary Material provides comparisons of the rain estimates of the different products for each category.

IMERG Products

Figures 11a,b and 12a,b provide the rain accumulations estimated for our both case studies by EARLY and LATE products, respectively. The rain distribution over France was quite similar using either the EARLY or the LATE product for each of the case studies (Figures 11a and 12a for the April case, and Figures 11b and 12b for the June case). Locally, few differences appeared, such as precipitation fields that were more intense in EARLY than in LATE over the northern Alps and the Cévennes for the April case, and the precipitating band that seems more extended over the northeastern part of France in EARLY than in LATE for the June case.

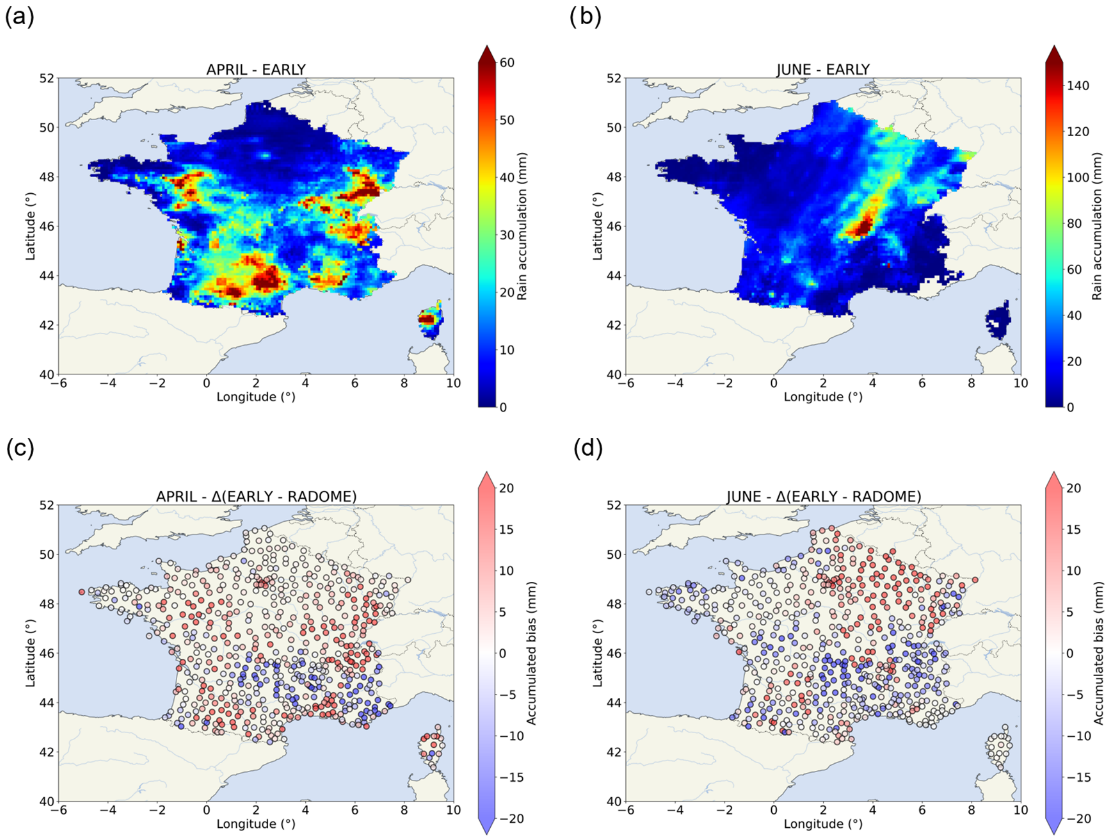

Figure 11. As in Figure 4, but for rain accumulations estimated by the IMERG-Early product.

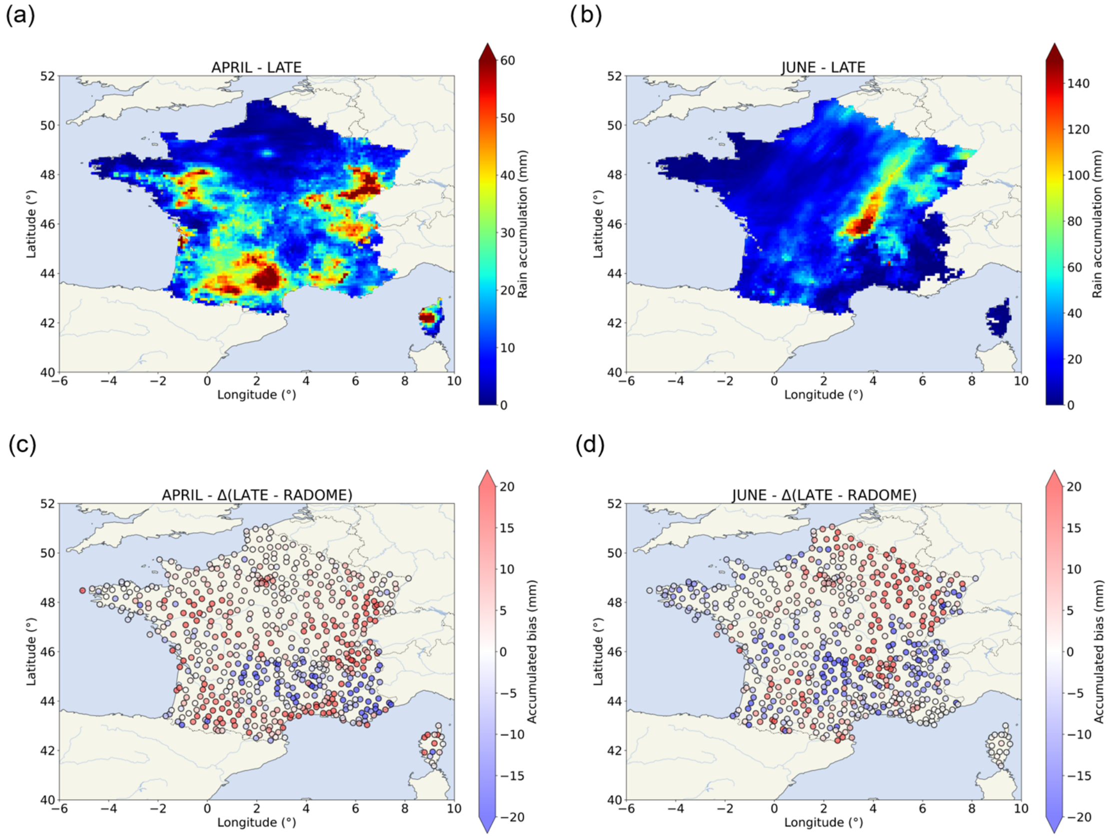

Figure 12. As in Figure 4, but for the IMERG-Late product.

For the April case (Figures 11a,c and 12a,c), the most intense rainfall was localised over the same specific areas defined in Figure 2c. However, they seemed to be shifted compared to the rain-gauge observations (Figure 2a). For example, the most precipitating cells were located further south within the WMC area, whereas they were located further north within the DUR and SAL areas. Moreover, important rain amounts (higher than 50 mm) were also estimated over the northwestern part of France using both IMERG products, while the rain gauges did not measure such quantities over this region. Tables 2 and 3 show that the EARLY and LATE rain amounts were close to the RADOME observations for the WMC but that they were slightly shifted spatially, since the rain maximum estimated for EARLY and LATE was located at approx. 15 km to the observed one. Additionally, Figures 11c and 12c show that an underestimation by the IMERG products was present over the southern part of WMC, whereas an overestimation was present over the northern part (this spatial shift induces the quite low mean absolute biases obtained for this specific area; Table 3). Nonetheless, the IMERG products can highly overestimate the rain amounts as for the JUR area (where the mean absolute biases are +20.87 mm for EARLY and +24.69 mm for LATE; see Table 3). In the opposite, EARLY and LATE can also produce important underestimations, such as for the SAL area (where the mean absolute biases reach −15.51 mm and −14.99 mm, respectively). For this case, the IMERG products had difficulties in estimating the rain amounts over the reliefs of the south of France, especially over the Alps (DUR and SAL) and the Jura (JUR), but also along the Mediterranean coast.

For the June case (Figures 11b,d and 12b,d), the more important rain amounts are mainly located over the NMC area as in RADOME observations but the maxima of rain obtained by either EARLY or LATE are approx. 2 times higher than measured by the rain gauges (the rain maximum was 136.7 mm in RADOME while it is equal to 223.86 mm and 211.99 mm for EARLY and LATE, respectively; see Table 2). These maxima are located at approx. 70 km further east than the Chastreix station (where the RADOME maximum is observed). Figures 11b and 12b also reveal moderate rain amounts over the northeastern part of France (in the vicinity of the Belgium and Luxembourg borders) in both IMERG products, which were not visible in the RADOME observations (Figure 2b), inducing positive biases over this region (Figures 11d and 12d). As the most intense precipitation amounts were estimated further east than observed, this entails an underestimation over the western part of the NMC in both IMERG products (negative biases), whereas this was the opposite in the eastern part (positive biases). Thus, the mean absolute biases (Table 3) obtained for EARLY and LATE products were quite small for this specific area: −4.55 mm and −0.58 mm, respectively.

The two IMERG products provide similar precipitation estimations for both case studies. However, we can notice that LATE showed greater values of precipitation accumulations than EARLY for both cases (see Table 3). Initially, in the study of O et al. [52] over southeastern part of Austria, using the WegenerNet rain-gauge gridded dataset as a reference, the authors found that the backward morphing scheme of IMERG-Late (V03) had only little effects compared to the simple forward scheme of IMERG-Early (V03). Furthermore, in their study they marked that EARLY and LATE tended to overestimate low rain rates, such as is observed with the case study over the JUR area and, inversely, that high-intensity precipitation amounts were underestimated by the IMERG family, as is observed over the NMC area during the June case.

CMORPH Products

The precipitation accumulations estimated for both case studies by CMORPH-RT and CMORPH are shown in Figures 13a,b and 14a,b (Table 1 resumes the products features). The identification of the high-density precipitation patterns was similar for both products for both case studies. The differences appear when we compare the "pixelated" aspect of CMORPH-RT precipitation patterns (such as over the JUR area) to the smoother aspect of CMORPH during the April case (Figures 13a and 14a, respectively). CMORPH-RT identified more intense precipitation patterns over JUR, the north of the Alps and the southwestern parts of France than CMORPH for the April case. However, CMORPH-RT estimated a less intense precipitation band for the June event than CMORPH (see Figures 13b and 14b).

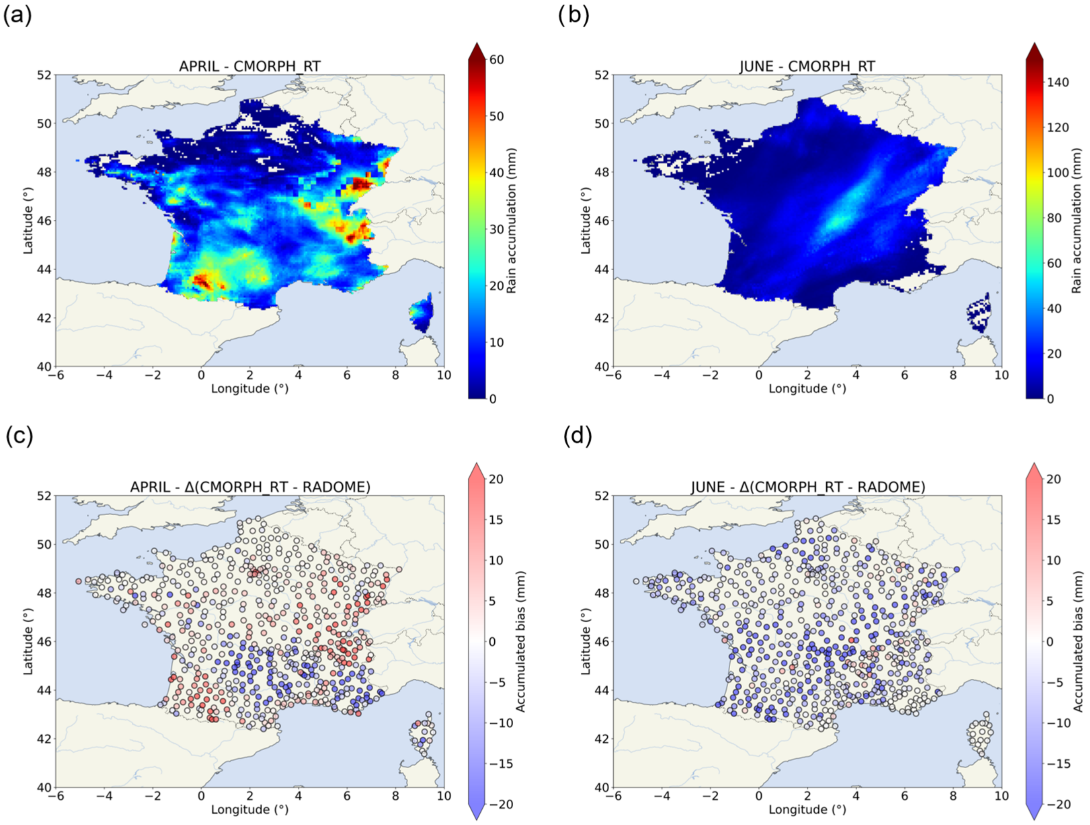

Figure 13. As in Figure 4, but for rain accumulations estimated by the CMORPH-RT product.

The representation of precipitation patterns was similar with the two products for the April case (Figures 13a,c and 14a,c), but differences in quantification were observed locally. Over the WMC area, CMORPH-RT (Figure 13a) located the high-intensity precipitating cells outside the area, with a southwest shift. In comparison, the position of the most-intense precipitation amounts estimated by CMORPH (Figure 14a) was located close to RADOME's maximum over the WMC area. Close to the JUR area, CMORPH-RT showed pixel clusters with very-low-intensity precipitation amounts adjacent to moderate- to high-intensity precipitating cells not observed with RADOME (Figure 2a). CMORPH represents the precipitation pattern over this area with a much smoother appearance. We can see high-intensity estimations over the northern parts of the Alps. However, very-low-intensity precipitation amounts over the SAL and DUR areas were identified by both products, revealing a northern spatial shift over the Alps. Table 2 confirms the shifted location of the precipitation accumulation maximum of CMORPH-RT compared to the RADOME counterparts. However, we can note that the CMORPH maximums were closer to RADOME ones than CMORPH-RT, with the only exception being the JUR area. By looking at the spatial bias distribution (Figures 13c and 14c), we can see a large underestimation trend across the Southern parts of the country for both products, especially over the SAL, DUR, and WMC. This trend is confirmed when we see the negative biases computed over these areas (Table 3). However, over the JUR area, we can note that CMORPH-RT estimations overestimated RADOME by +12.84 mm on average, while for CMORPH the average difference was close to 0 mm.

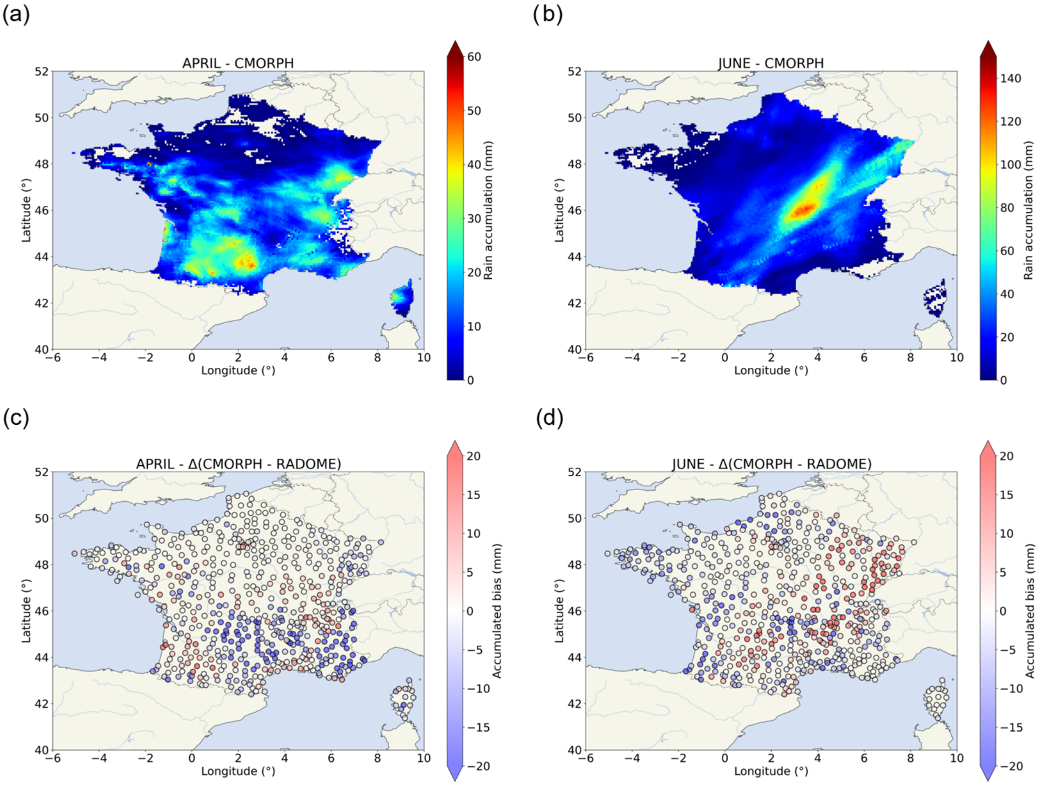

Figure 14. As in Figure 4, but for the CMORPH product.

The June case (Figures 13b,d and 14b,d) was extended from the NMC area to the northeast of the country for both products. The main difference was in the quantification of the event, as CMORPH-RT estimated a small area of moderate precipitation intensity (less than 60 mm), while CMORPH estimated higher precipitation amounts closer to the RADOME observations. As seen in Table 2, the maximum estimated by CMORPH-RT was around 2 times lower than the RADOME maximum over NMC, whereas CMORPH had a similar maximum compared to the RADOME counterpart. However, this CMORPH maximum was located 83.22 km to the east of the Chastreix station against the 46.20 km separating Chastreix to the CMORPH-RT maximum. In Figure 13d and Table 3, we can see the strong underestimation trend observed with CMORPH-RT over the NMC and France. In contrast, CMORPH (Figure 14d) overestimated at locations around the centre of the NMC area, leading to a slight positive bias on average (+1.25 mm).

The rainfall patterns estimated by the two CMORPH versions present some differences at the local scale. CMORPH-RT estimations were highly heterogeneous in some areas such as JUR during the April event. CMORPH-RT is a real-time product and has to wait for the next PMW estimation from the satellite flyby to update its estimations [47]. Moreover, CMORPH-RT applied only a forward propagation at the time of the precipitation fields once estimated by PMW satellites without modifying the intensity or the shape [47]. The strong underestimation experienced by CMORPH-RT can be attributed to the CMORPH-RT simple-shot. The June case was convective and thus contained a rainfall regime with a rapidly changing structure, which may have been missed by CMORPH-RT, as it had to 'wait' for the next PMW sensor estimation. Despite finding negative biases over the areas of interest with both products, the spatial representation of both cases by CMORPH were closer to the RADOME observation than CMORPH-RT. CMORPH represented both case studies with a smoother appearance due to its morphing algorithm (see Section 2.1.3).

GSMaP Products

The rain accumulations estimated for both April and June case studies are presented in Figure 15a,b for GSMaP-Now, Figure 16a,b for GSMaP-Now-GC, Figure 17a,b for GSMaP-NRT, and Figure 18a,b for GSMaP-NRT-GC (the details of GSMaP family products are presented in Table 1 and Section Microwave Sensor-Based and Blended Products). The differences between GSMaP-Now and GSMaP-Now-GC (Figures 15a and 16a for April and Figures 15b and 16b for June) were mainly limited to the intensity of the events regionally. A similar statement can be made about the differences noted between GSMaP-NRT and GSMaP-NRT-GC for both case studies (Figures 17a and 18a for April and Figures 17b and 18b for June). The distribution of the absolute bias of GSMaP-Now products and GSMaP-NRT products is represented in Figures 15c,d and 16c,d; and 17c,d and 18c,d, respectively.

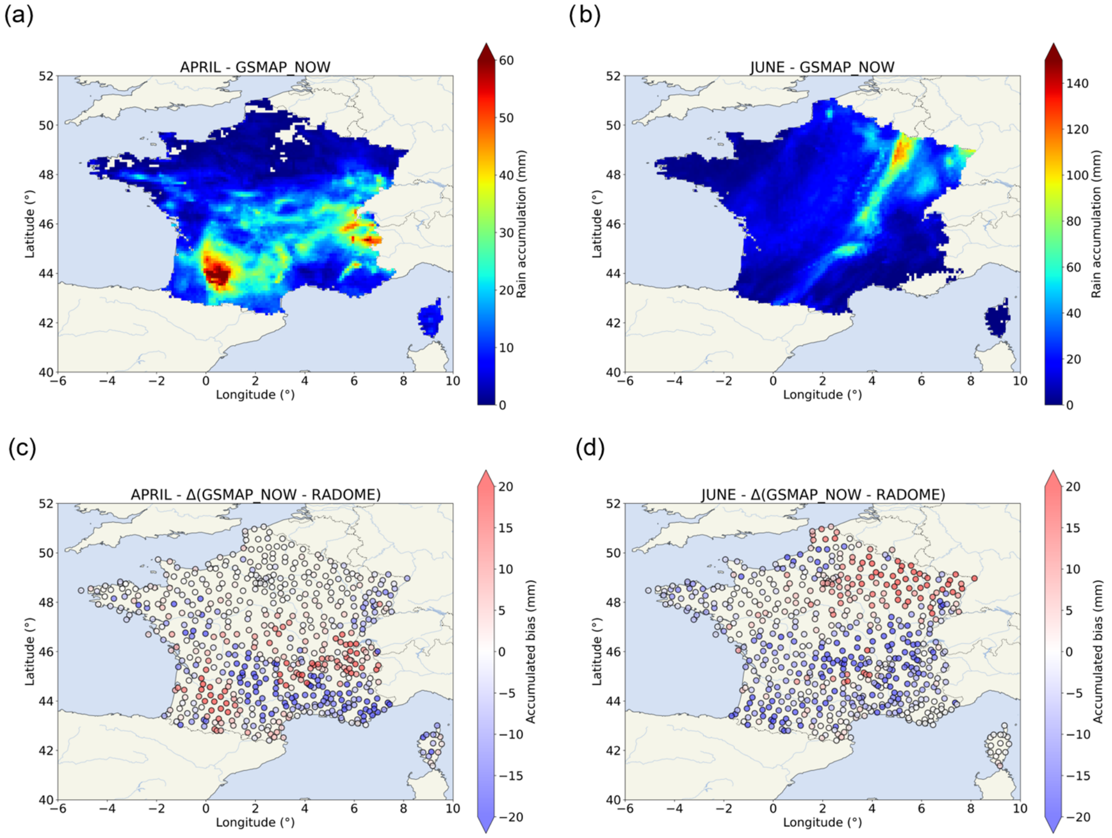

Figure 15. As in Figure 4, but for rain accumulations estimated by the GSMaP-Now product.

For GSMaP-Now products during the April case (Figures 15a,c and 16a,c), the most intense precipitation pattern was located over the west border of the WMC area. Another area of high-intensity precipitation pattern was located in the north of the Alps, whereas moderate-intensity precipitation amounts (between 15 to 30 mm) were observed by RADOME. Both these high-intensity precipitation patterns have a westerly shift (for the WMC area) and a northerly shift (for the Alps) compared to the RADOME observations (Figure 2a). For every area, the distance from both GSMaP-Now products' maximums to RADOME maximums were identical, regardless of the effect of the gauge adjustment (Table 2). Furthermore, it is important to note that the minimal distance separating both maximums was approx. 80 km, marking the difficulty of both GSMaP-Now products to correctly identify the location of each maximum. By looking at the distribution of absolute biases (Figures 15c and 16c), we can see that a large area of underestimation extended from the south of the Alps westward to the eastern part of the WMC area.

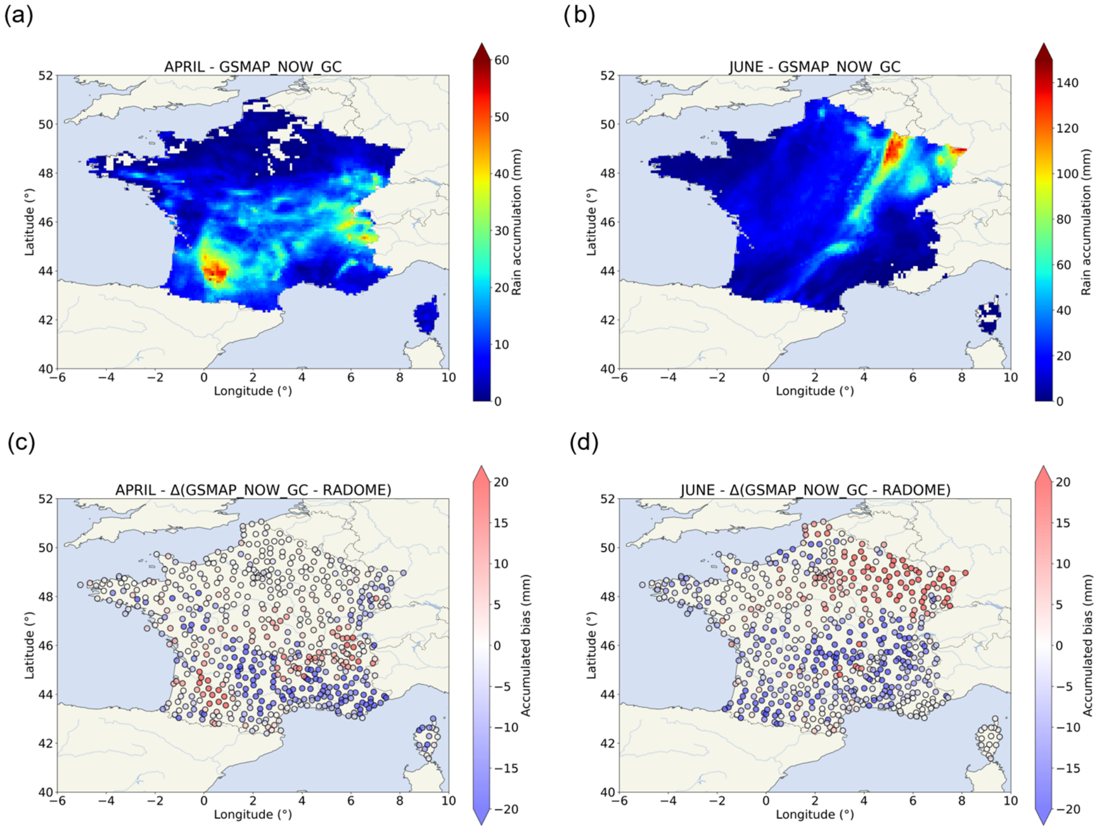

Figure 16. As in Figure 4, but for the GSMaP-Now GC product.

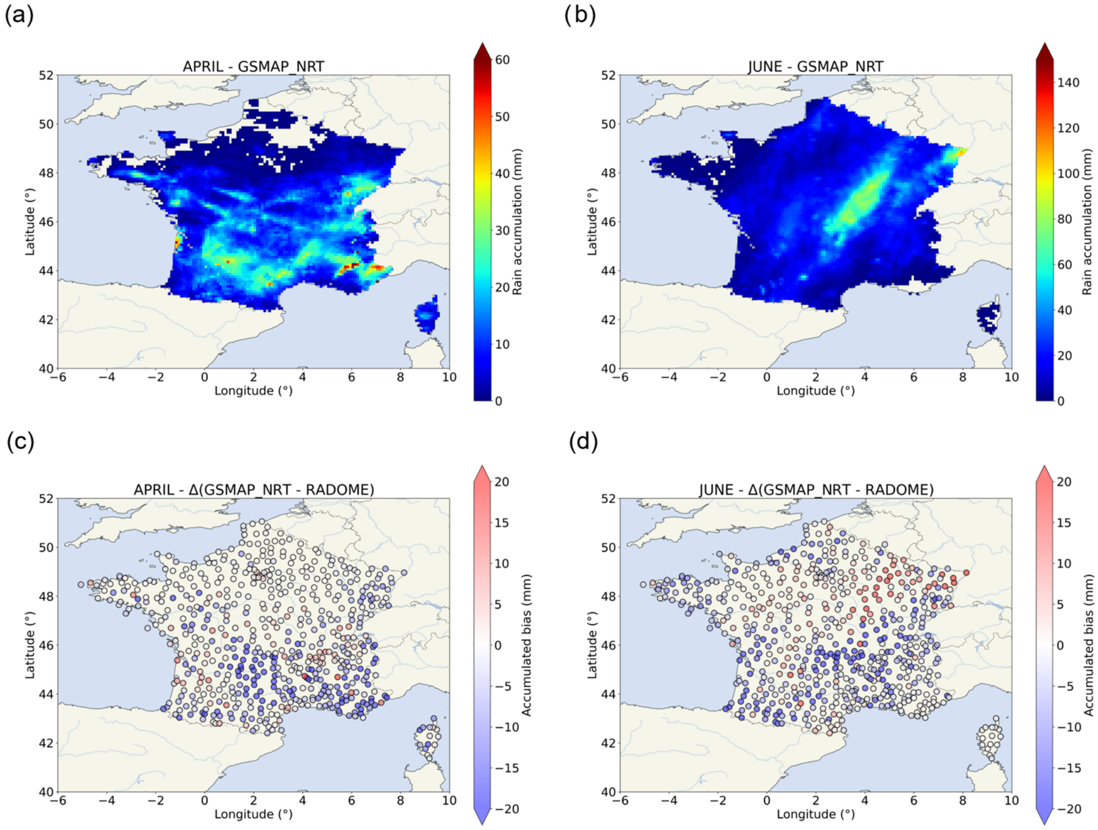

Figure 17. As in Figure 4, but for the GSMaP-NRT product.

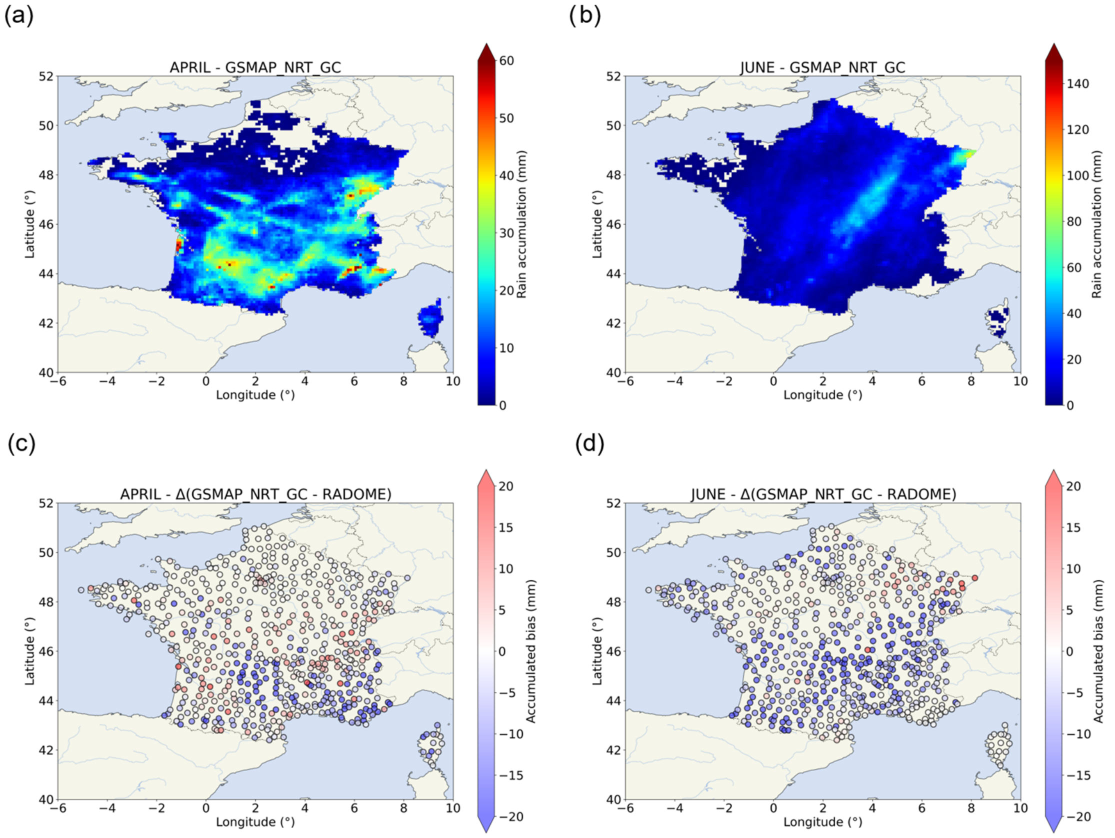

Figure 18. As in Figure 4, but for the GSMaP-NRT GC product.

We can see the first overestimation pattern was identified in the north of the Alps confirming a northern shift in the high-intensity precipitation amounts observed by RADOME over the South Alps areas. A second overestimation signal was present in the west of the WMC area, confirming a western shift of the high precipitation amounts observed over the WMC area. This leaves a general underestimation trend for both GSMaP-Now products over the study areas (ranging from −3.69 mm over the WMC to −21.05 mm over SAL on average for GSMaP-Now and from −5.54 mm over JUR to −24.44 mm over SAL on average for GSMaP-Now-GC).

As for the June event (Figures 15b,d and 16b,d), GSMaP-Now and GSMaP-Now-GC reproduces the high-intensity rainfall patterns close to the borders with Belgium and Germany (Figures 15b and 16b). We can observe low-intensity precipitation amounts and low maximums for both products over the NMC area (82.83 mm for GSMaP-Now and 82.43 mm for GSMaP-Now-GC against 136.7 mm for RADOME; Table 2). Both products' maximums were separated to the same distance of 126.89 km from the Chastreix station. These most-intense precipitation amounts estimated in northeast France showed a strong overestimation mark, while within the NMC both GSMaP-Now showed strong underestimation signals (Figures 15d and 16d). The quantification of these biases shows a negative −19.63 mm for GSMaP-Now and −20.57 mm for GSMaP-Now-GC, on average, over the NMC area (Table 3).

The distribution of GSMaP-NRT and GSMaP-NRT-GC estimations (Figures 17a and 18a) showed moderate- to high-intensity precipitation amounts over every area of interest close to the RADOME observations. At the local scale, the highest precipitation amount was located over the Alps, especially over the DUR and SAL area with maximums reaching 85.73 mm for GSMaP-NRT and 84.53 mm for GSMaP-NRT-GC (Table 2). Furthermore, we can see that the distance separating both GSMaP-NRT versions' maximums from the RADOME counterpart is identical (Table 2). However, both products had difficulties in correctly localising the RADOME maximum during the April case, as these distances were varied from 57.61 km within the DUR area to 132.31 km within the WMC area. The high precipitation amounts over the WMC were shifted to the west. Despite a good representation of the rain patterns, the medians of both GSMaP-NRT estimations over the areas of interest were mainly lower than the RADOME median (Table 3). As seen in Figures 17c and 18c, the spatial distribution of the absolute bias between the estimations of both versions of GSMaP-NRT and the RADOME observations shows strong underestimation signals across the south of France. These negative biases ranged from −3.72 mm over JUR to −14.06 mm over SAL for GSMaP-NRT and from −6.51 mm over CEV to −16.78 mm over GSMaP-NRT-GC. Only GSMaP-NRT-GC had a small area of overestimation located over the JUR area (+3.84 mm in average).

For the June case (Figures 17b and 18b), the precipitation pattern estimated by both GSMaP-NRT products extended from the NMC area to the border with Germany, agreeing with the RADOME observations. The intensity of the precipitation pattern over the NMC area indicates that GSMaP-NRT products estimated moderate- and low-intensity precipitation amounts (approx. 80 mm for GSMaP-NRT and approx. 50 mm for GSMaP-NRT-GC). In fact, Table 2 reveals that the maximum within NMC area was evaluated to be 83.97 mm with GSMaP-NRT and 51.15 mm with GSMaP-NRT-GC, much lower than the RADOME maximum (136.70 mm). Both maximums were located at a distance of 77.85 km from the northeast of the Chastreix station where the RADOME maximum is recorded. By looking at the spatial distribution of the absolute biases for both GSMaP-NRT versions (Figures 17d and 18d), we can see a strong underestimation signal, which is more defined with GSMaP-NRT-GC. This is confirmed as the precipitation estimation median inside the NMC was lower than RADOME (26.02 mm for GSMaP-NRT and 15.85 mm for GSMaP-NRT-GC against 35.7 mm for RADOME; Table 3) and quantified at −15.73 mm for GSMaP-NRT and −26.17 mm for GSMaP-NRT-GC.

These results show that GSMaP-Now and its gauge-adjusted version did not correctly identify the position of both the case studies, unlike GSMaP-NRT which identified the precipitation fields observed by RADOME. GSMaP-Now showed underestimation signals compared to the rain-gauge reference, which tended to be reduced with the gauge adjustment. In contrast, GSMaP-NRT identified the precipitation events, and the distance between the GSMaP-NRT (and GSMaP-NRT-GC) and RADOME maximums were smaller than the one found with the GSMaP-Now products. Both GSMaP-Now and GSMaP-NRT products presented small differences compared to their respective gauge-adjusted versions but these differences were not uniform and varied at the local scale (e.g., the decrease in estimated values from GSMaP-NRT to GSMaP-NRT-GC during the April case; Table 3). With the 8th version of GSMaP, Ramadhan et al. [51] concluded that the performance of both GSMaP-Now products is poorer than the performance of GSMaP-NRT, and that this can be associated with a more complete satellite coverage and merging method.

3.2.3. C/N-Based Product

Figure 19a,b presents the precipitation amounts estimated by DATABOURG during both the April and June case studies. The DATABOURG product uses an innovative method to estimate and process precipitation at high spatial and temporal resolutions as described in Section 2.1.3. No similar observations–estimations comparison at this spatial scale has been conducted by using DATABOURG estimations but it has been previously found that the dataset is closer to rain-gauge observations than the estimations of the German DWD radars of Neuheilenbach [22].

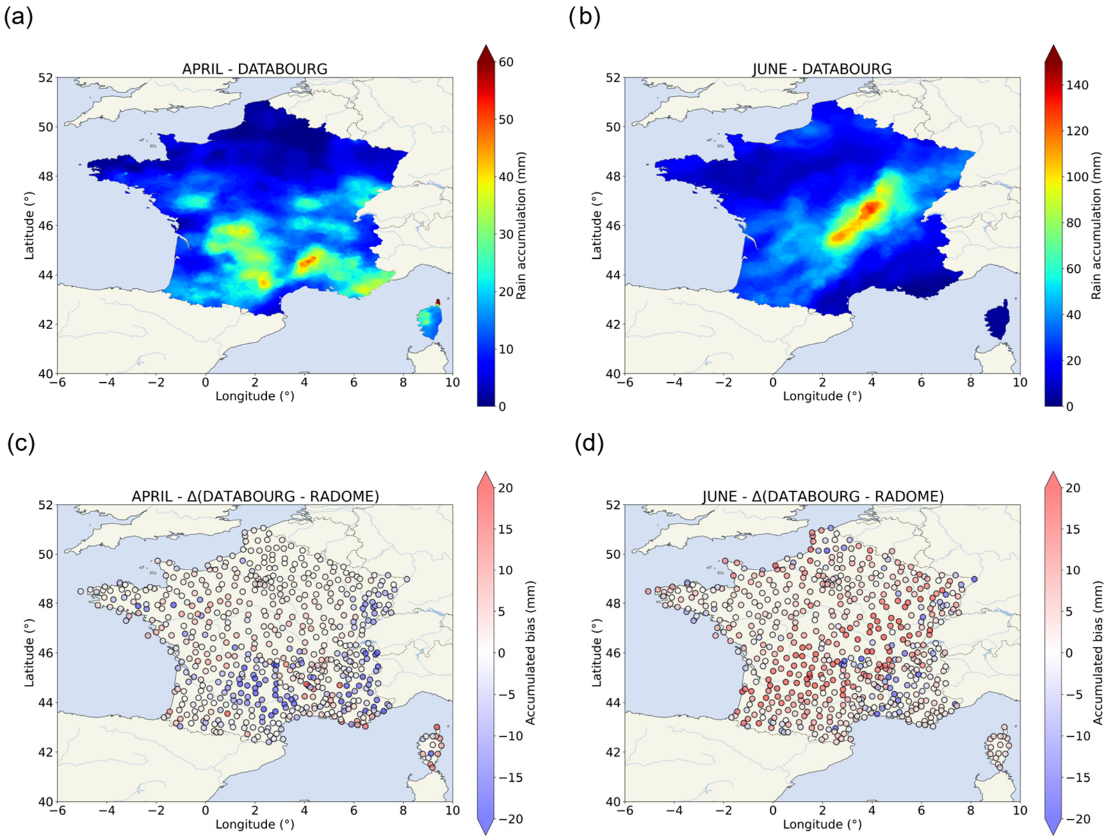

Figure 19. As in Figure 4, but for the DATABOURG product.

For the April case (Figure 19a,c), DATABOURG estimated moderate- to high-intensity precipitation amounts over the south of France, most notably over the WMC, SAL, and CEV areas. The locations of the precipitation patterns agree well with the observations made by RADOME (Figure 2a). Moreover, the distance between the maximum estimated by DATABOURG and the maximum observed by RADOME was less than 20 km for the WMC, DUR, and CEV areas (Table 2). However, the DATABOURG maximums were lower than the RADOME maximums by more than 20 mm (Table 2). An exception concerns the DATABOURG maximum over the JUR area being close to the observation but this was located 108.96 km away from its RADOME counterpart. In Figure 19c, we can identify an area of underestimation across the eastern part of the WMC area and the areas located in the east of the country. Over the northeastern part of the CEV area, a local overestimation area was detected, corresponding to the highest-intensity precipitation amounts estimated by DATABOURG. The medians of the DATABOURG estimations inside each area of interest (Table 3) were lower than the medians of the RADOME observations by less than 7 mm, confirming the underestimation observed previously. The mean absolute biases (Table 3) confirm the presence of a slight underestimation over the study areas (ranging from −3.11 mm over CEV to −6.83 mm over the WMC area).

The DATABOURG estimations for the June case (Figure 19b) reveal an area of high-intensity precipitation amounts (more than 110 mm) extending from Central to northeast NMC area. A larger moderate-intensity precipitation amount (more than 60 mm) surrounded the latter in a southwest–northeast axis, matching the RADOME observation, although these areas were more extensive than their RADOME counterparts. The difference appeared in the extent of the high-intensity precipitation pattern estimated by DATABOURG, as the distance separating the DATABOURG maximum and the RADOME maximum was 157.18 km (Table 2) further to the northeast, despite having a very close maximum to the observation. In Figure 19d, we can see the large overestimation pattern linked to the extent of high-intensity rainfall estimations from the DATABOURG compared to RADOME observations. Over the NMC, the median of the accumulated precipitation estimated by DATABOURG was more than 14 mm over the one computed by RADOME (Table 3). This overestimation pattern was +8.94 mm, on average, over the NMC.

4. Discussion

In this study, multiple radar and satellite precipitation products with different spatial and temporal characteristics were compared to a rain-gauge network (RADOME) over mainland France during two rainfall case studies over 3- and 4-day periods. Every area of interest studied concerned mountainous regions of the south and the east of France, such as the French Alps (the SAL and DUR areas), the Jura (the JUR area), and the Massif Central (the CEV, WMC, and NMC areas) massifs. Hence, the study was conducted over complex topography. The precipitation products were compared using the point-to-pixel method, which provided absolute bias between the product's estimations and observations from the rain-gauge network RADOME. Figure 20 represents the distributions of the absolute bias computed for each product against the rain-gauge observations for every specific area of interest.

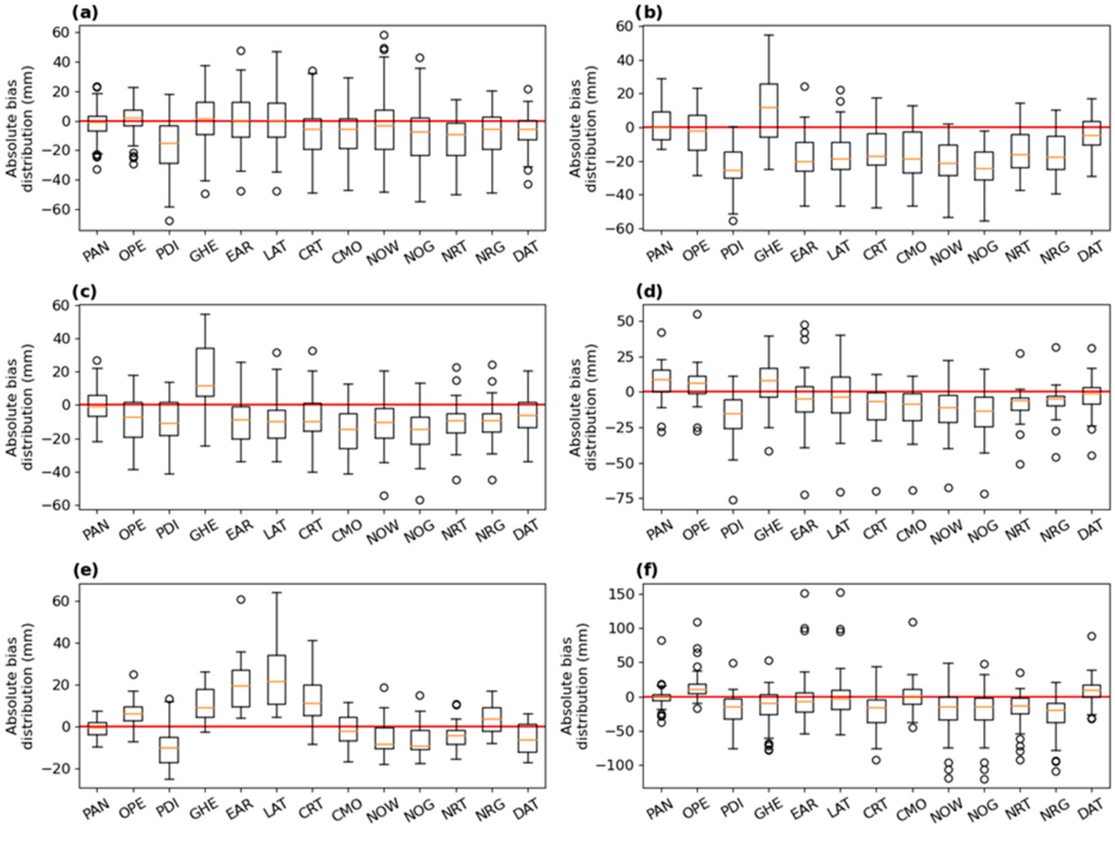

Figure 20. Distribution of the absolute biases computed at the stations by using the point-to-pixel method inside the specific areas presented in Figure 2c for the April (**a**–**e**) and June cases (**f**). The corresponding areas are as follows: WMC (**a**), SAL (**b**), DUR (**c**), CEV (**d**), JUR (**e**), and NMC (**f**). The boxes correspond to the interquartile range of the absolute bias distribution, with the lower and upper end of the boxes being, respectively, the 1st and 3rd quartiles of the distribution. The orange lines are the medians of the distributions. The whiskers go to the last value point within 1.5 times the interquartile range. Outliers are identified with a small circle. The solid red line represents the equation y = 0.

Concerning the ground-based radar estimations, the results show that both PANTHERE and OPERA provided a good spatial representation of the events and PANTHERE had the lowest biases regardless of the case studies. Figure 20 shows that the median of the absolute biases was very small (close to 0 mm) over the different areas of interest, confirming the performance of the product seen in Section 3.1.2. Figure 20 also shows the tendency of OPERA to slightly overestimate the precipitation amounts compared to RADOME, with notable exceptions over the areas within the Alps where a slight underestimation was recorded as seen in Section 3.1.3. This underestimation experienced by OPERA over the Alps area can be attributed to the lack of radar coverage in this specific area. Due to differences in sampling volume, it was possible to find biases between radar and rain gauge in one direction or the other. For example, Schleiss et al. [69] found a underestimation of radar data compared to rain gauge of 10% in a study over northern Europe. Di Curzio et al. [70] also found a general underestimation in Abruzzo and Marsica regions in Italy. In contrast, the overestimation signal estimated over the JUR area tended to be linked with the contribution of the German radars. The strongest differences experienced by both products were observed over the mountainous areas of the south of France, revealing the difficulties for radar products to correctly estimate precipitation over area with complex topography. The OPERA overestimation trend was also observed during the June case.

As for the satellite-based products, we can see in Figure 20 that they generally tend to underestimate precipitations amounts. This type of event was not well represented by PDIR, which can be explained because IR-based products tend to fail to correctly estimate low-intensity rainfall and orographic events [12]. GHE tends to overestimate the precipitation over multiple areas, which could be explained because of the fixed algorithm, based on brightness temperature, to retrieve rain amounts (Section 2.1.3). Both IMERG products showed similar results and, thus, showed the small effects of the forward and backward morphing of LATE (see Section 3.2.2). Figure 20 shows that the bias distributions of LATE were larger than EARLY in most of the areas of interest. This could indicate that the dispersion of the absolute bias values was greater with LATE than EARLY. Hence, in our case, EARLY showed better results despite being the IMERG product with the shortest latency. For the CMORPH family, the results were similar in the identification of both events; however, the quantification of the precipitation amounts revealed some differences locally (CMORPH-RT close to the JUR area during the April case; Section 3.2.2). Figure 20 shows that CMORPH tends to have more absolute biases close to 0 mm than CMORPH-RT, meaning that CMORPH estimations are closer to RADOME observations than CMORPH-RT. Figure 20 also shows that GSMaP-NRT products tend to have smaller absolute bias distributions and are more centred around 0 mm, supporting the results seen in Section 3.2.2. The GSMaP family products tend to underestimate the precipitation amounts compared to the RADOME observations, as well as for the rest of the MW-based precipitation products. Finally, the DATABOURG product shows relatively small bias distributions near 0 mm but a notable underestimation of the April case, while the June case was marked by an overestimation signal.

In our case, both radars products showed good performances over France. For the satellite-based products, DATABOURG shows promising results while CMORPH and both IMERG products correctly identified both events. However, GSMaP-Now products and PDIR estimations tend to show poorer results. With the difficulty for PDIR to correctly identify and quantify the precipitation amounts on both events, this study confirms that products with finer spatial resolution do not always produce better representations of precipitation events, as found in the work of Llauca et al. [62]. This study also shows that all precipitation products tend to have difficulty in correctly estimating stratiform and light precipitation events over areas with high topography (e.g., [71]), such as in the case of the April case study. Topography has an important role in the contribution of precipitation on high mountainous areas, which are of particular interest for global climate projections [72].

5. Conclusions and Perspectives

In this article we presented a detailed analysis of the different precipitation products currently available (satellite and radar), through two case studies in which we quantified and analysed the differences in rainfall observations. The products have different spatiotemporal characteristics and processing methods for assessing the retrieval of ground-radar reflectivity or brightness temperature to obtain rain-rate estimations

First, we present comparisons between radar products against the rain-gauge network over France. Both PANTHERE and OPERA show very satisfying performances over France, with PANTHERE having the lowest biases on average over France for both case studies. The main differences are observed over the complex topography of the south of France, where the highest precipitation amounts are observed. OPERA does not include the X-band radar over the Alps, leading to an underestimation over the area. The presence of the Swiss and German radars near the border influences the estimation of the precipitation around the Jura area by OPERA. Finally, OPERA estimated higher precipitation amounts than the observed values for both case studies. Nevertheless, the high spatiotemporal and very-short-latency characteristics of both products remain very interesting for nowcasting applications over France, for example.

Then, we compare the behaviour of 11 satellite precipitation products against the observations made by RADOME over France during the two case studies. With the sole exception of DATABOURG, we should remind you that the satellite-based products have the benefits of covering a wide portion of the Earth's surface. In our case, these satellite products have the benefits of a near-real-time latency and showing good representation of high-intensity precipitation events, such as the June case. The main conclusions are as follows:

- PDIR and GHE found difficulty in identifying the position of the April event but correctly detected the June event. The IR-based technique might be well adapted for these more convective conditions with high spatial (4×4 km^2) and temporal (15 min to 1 h) resolutions with relatively short latency (minutes to hours);
- Short-latency (real-time) MW-based products tend to produce worse representations of the precipitation cases such as CMORPH-RT and GSMaP-Now products. GSMaP-Now products had difficulty in representing the event but the quantification was coherent with the RADOME observations;
- In comparison, GSMaP-NRT performed better than GSMaP-Now in the detection of the event, especially in the identification of the June event;
- A similar statement can be made about the reprocessed CMORPH version compared to the heterogeneity in precipitation amounts' quantification by CMORPH-RT. The morphing method allowed for a better representation and quantification of both case studies;
- The gauge-adjustment effectuated for the GSMaP-Now-GC and GSMaP-NRT-GC did not show a significant improvement in the quantification of both events;
- IMERG-Early and IMERG-Late showed a trend to slightly overestimate the presence of rain, as shown by the overestimation recorded at low-rain-amount areas. They also tend to underestimate high rain-rate values but they well represented both case studies over the south regions of France;
- The reprocessing applied to IMERG-Late does not improve the estimations compared to IMERG-Early;
- CMORPH-RT showed traces of raw LEO satellite observation swaths over parts of the country. This was traduced by strong differences at the very-local scale, over the JUR area for example. CMORPH-RT showed low bias medians but CMORPH was better at the spatial representation of both events;
- Despite slightly overestimating during the June event, DATABOURG showed promising results with low biases for both cases with the highest spatiotemporal resolution (1 km^2 and 5 min).

PANTHERE gives closer results to rain gauges than OPERA for radar precipitation product, DATABOURG shows the most promising results with low biases over parts of France, and this dataset can be used for nowcasting applications. Additionally, CMORPH, both IMERG products and both GSMaP-NRT products, showed really good representation of both events. The short-latency products (PDIR, GHE, CMORPH-RT, and GSMaP-Now products) showed poorer results but can be used to monitor fast-moving precipitation events. Ideas to combine the high spatiotemporal resolution characteristics of IR-based products and the higher precision of MW-based products can be explored further. It is worth noting that the differences between the products of the same family (IMERG, GSMaP-Now, GSMaP-NRT, and CMORPH) were not so marked. From the results shown, we can conclude that it is not essential to wait for the product with the highest latency for a nowcasting application. However, further studies over a longer period of time are advised.

Regarding perspectives for this study, other more-adapted spatialized metrics should be exploited in order to better quantify the representation of rain events, such as the use of the Probability of Detection, the False Alarm Ratio, or the Critical Success Index. This study can also be performed by using other methods of comparison such as the pixel-to-pixel method by interpolating the observed rain rates to a gridded dataset or by using Kriging methods. But this work must be conducted after a careful reflection on the remapping or interpolation method used to obtain the identical grid for all products. Further studies are also encouraged to conduct over a longer study period, over more case studies, or even over other study areas in order to test the robustness of the conclusion's made on the performance of satellite precipitation products.

Supplementary Materials: The following supporting information can be downloaded at: https://www.mdpi.com/article/10.3390/atmos14121726/s1, Figures S1–S6 represents the local differences in the rain amounts and distributions obtained with IMERG-Early and IMERG-Late (Figure S1), CMORPH-RT and CMORPH (Figure S2), GSMaP-Now and GSMaP-Now-GC (Figure S3), GSMaP-NRT and GSMaP-NRT-GC (Figure S4), GSMaP-Now and GSMaP-NRT (Figure S5) and GSMaP-Now-GC and GSMaP-NRT-GC (Figure S6).

Author Contributions: Conceptualization, J.-L.B., C.P., E.B. and A.C.; methodology, J.-L.B., C.P. and A.C.; software, A.C.; validation, J.-L.B., C.P., E.B. and A.C.; formal analysis, J.-L.B., C.P. and A.C.; investigation, J.-L.B., C.P. and A.C.; resources, J.-L.B., C.P. and E.B.; data curation, A.C.; writing—original draft preparation, J.-L.B., C.P. and A.C.; writing—review and editing, J.-L.B., C.P., E.B. and A.C.; visualization, A.C.; supervision, J.-L.B., C.P. and E.B.; project administration, J.-L.B., C.P. and E.B.; funding acquisition, J.-L.B., C.P. and E.B. All authors have read and agreed to the published version of the manuscript.

Funding: The MAPS project is funded by the France Relance Préservation de l'emploi de Recherche et Développement programme of the French Research Agency (ANR) and the company Weather-Measures under the grant number (ANR21-PRRD-0009-01).

Institutional Review Board Statement: Not applicable.

Informed Consent Statement: Not applicable.

Data Availability Statement: Publicly available datasets are analysed in this study and available via the links below: GHE data: https://www.noaa.gov/nodd/datasets, accessed on 19 November 2023; PDIR data: ftp://persiann.eng.uci.edu/CHRSdata/PDIRNow, accessed on 19 November 2023; IMERG data: https://doi.org/10.5067/GPM/IMERG/3B-HH-E/06, accessed on 19 November 2023 for IMERG-Early and https://doi.org/10.5067/GPM/IMERG/3B-HH-L/06, accessed on 19 November 2023) for IMERG-Late; CMORPH data: http://ftp.cpc.ncep.noaa.gov/precip/CMORPH_RT/, accessed on 19 November 2023 for CMORPH-RT; https://ftp.cpc.ncep.noaa.gov/precip/CMORPH_V0.x/, accessed on 19 November 2023 for CMORPH; and https://sharaku.eorc.jaxa.jp/GSMaP/, accessed on 19 November 2023 for GSMaP data. The ERA5 reanalysis used in this study was provided by the ECMWF (https://doi.org/10.24381/cds.adbb2d47, accessed on 19 November 2023 and https://doi.org/10.24381/cds.bd0915c6, accessed on 19 November 2023) and generated using Copernicus Climate Change Service (C3S). DATABOURG, PANTHERE, RADOME, and OPERA datasets are available on request to corresponding authors.

Acknowledgments: We acknowledge the technical and scientific staff of LaMP and Weather-Measures for their helpful discussions and management. We acknowledge the Databourg Systems staff for their help in the providing the exploitation of the DATABOURG datasets. We acknowledge the NESDIS Data access staff of NOAA for their help in GHE exploitation. We acknowledge the OPERA database service.

Conflicts of Interest: The authors declare no conflict of interest.

Abbreviations

AMW	Active MicroWave
ARAMIS	Application Radar À la Météorologie Infra-Synoptique
C/N	Carrier-to-Noise
CEV	Cévennes
CHRS	Center for Hydrometeorology and Remote Sensing
CMORPH	CPC MORPHing
CPC	Climate Prediction Center
DUR	Durance
EUMETNET	European METeorological NETwork
GEO	Geostationary Orbit
GHE	Global Hydro Estimator
GPM	Global Precipitation Measurement
GSMaP	Global Satellite Mapping of Precipitation
HE	Hydro Estimator
IMERG	Integrated Multi-satellitE Retrievals for GPM
IPCC	Intergovernmental Panel on Climate Change
IR	InfraRed
JAXA	Japan Aerospace Exploration Agency
JUR	Jura
LEO	Low Earth Orbit
MW	MicroWave
NASA	National Aeronautics and Space Administration
NESDIS	National Environmental Satellite, Data and Information Service
NMC	Northern Massif Central
NOAA	National Oceanic and Atmospheric Administration
NRT	Near Real Time
OPERA	Operational Program for Exchange of weather RAdar
PANTHERE	Projet ARAMIS Nouvelles Technologies en Hydrométéorologie Extension et REnouvellement
PCCS	PERSIANN Cloud Classification System
PCDR	PERSIANN Climate Data Record
PDIR	PERSIANN Dynamic Infrared Rain Rate
PERSIANN	Precipitation Estimation from Remotely Sensed Information using Artificial Neural Network
PMW	Passive MicroWave
R	Rain rate
RADOME	Réseau d'Acquisition de Données et d'Observation Météorologiques Etendues
RT	Real Time
SAL	Southern Alps
VPR	Vertical Profile of Reflectivity
WMC	Western Massif Central
Z	Reflectivity

References

1. Kidd, C.; Huffman, G.; Maggioni, V.; Chambon, P.; Oki, R. The Global Satellite Precipitation Constellation: Current Status and Future Requirements. *Bull. Am. Meteorol. Soc.* **2021**, *102*, E1844–E1861. [CrossRef]
2. Kundzewicz, Z.W.; Kanae, S.; Seneviratne, S.I.; Handmer, J.; Nicholls, N.; Peduzzi, P.; Mechler, R.; Bouwer, L.M.; Arnell, N.; Mach, K.; et al. Flood Risk and Climate Change: Global and Regional Perspectives. *Hydrol. Sci. J.* **2014**, *59*, 1–28. [CrossRef]
3. Volkert, H. Heavy Precipitation in the Alpine Region (HERA): Areal Rainfall Determination for Flood Warnings Through in-Situ Measureme Nts, Remote Sensing and Atmospheric Modelling. *Meteorol. Atmos. Phys.* **2000**, *72*, 73–85. [CrossRef]
4. Vicente-Serrano, S.M.; Beguería, S.; López-Moreno, J.I. A Multiscalar Drought Index Sensitive to Global Warming: The Standardized Precipitation Evapotranspiration Index. *J. Clim.* **2010**, *23*, 1696–1718. [CrossRef]

5. IPCC. *Climate Change 2022—Impacts, Adaptation and Vulnerability: Working Group II Contribution to the Sixth Assessment Report of the Intergovernmental Panel on Climate Change*; Pörtner, H.-O., Roberts, D.C., Tignor, M., Poloczanska, E.S., Mintenbeck, K., Alegría, A., Craig, M., Langsdorf, S., Löschke, S., Möller, V., et al., Eds.; Cambridge University Press: Cambridge, UK, 2023. [CrossRef]
6. Ren, M.; Xu, Z.; Pang, B.; Liu, W.; Liu, J.; Du, L.; Wang, R. Assessment of Satellite-Derived Precipitation Products for the Beijing Region. *Remote Sens.* **2018**, *10*, 1914. [CrossRef]
7. Paprotny, D.; Sebastian, A.; Morales-Nápoles, O.; Jonkman, S.N. Trends in Flood Losses in Europe over the Past 150 Years. *Nat. Commun.* **2018**, *9*, 1985. [CrossRef]
8. Cánovas-García, F.; García-Galiano, S.; Alonso-Sarría, F. Assessment of Satellite and Radar Quantitative Precipitation Estimates for Real Time Monitoring of Meteorological Extremes Over the Southeast of the Iberian Peninsula. *Remote Sens.* **2018**, *10*, 1023. [CrossRef]
9. Paranunzio, R.; Chiarle, M.; Laio, F.; Nigrelli, G.; Turconi, L.; Luino, F. New Insights in the Relation between Climate and Slope Failures at High-Elevation Sites. *Theor. Appl. Climatol.* **2019**, *137*, 1765–1784. [CrossRef]
10. Luino, F.; De Graff, J.; Roccati, A.; Biddoccu, M.; Cirio, C.G.; Faccini, F.; Turconi, L. Eighty Years of Data Collected for the Determination of Rainfall Threshold Triggering Shallow Landslides and Mud-Debris Flows in the Alps. *Water* **2020**, *12*, 133. [CrossRef]
11. Kidd, C. Satellite Rainfall Climatology: A Review. *Int. J. Climatol.* **2001**, *21*, 1041–1066. [CrossRef]
12. Sun, Q.; Miao, C.; Duan, Q.; Ashouri, H.; Sorooshian, S.; Hsu, K.-L. A Review of Global Precipitation Data Sets: Data Sources, Estimation, and Intercomparisons. *Rev. Geophys.* **2018**, *56*, 79–107. [CrossRef]
13. du Châtelet, J.P. Aramis, le réseau français de radars pour la surveillance des précipitations. *La Météorologie* **2003**, *40*, 44–52. [CrossRef]
14. Huuskonen, A.; Saltikoff, E.; Holleman, I. The Operational Weather Radar Network in Europe. *Bull. Am. Meteorol. Soc.* **2014**, *95*, 897–907. [CrossRef]
15. Kidd, C.; Levizzani, V. Status of Satellite Precipitation Retrievals. *Hydrol. Earth Syst. Sci.* **2011**, *15*, 1109–1116. [CrossRef]
16. Yu, L.; Leng, G.; Python, A.; Peng, J. A Comprehensive Evaluation of Latest GPM IMERG V06 Early, Late and Final Precipitation Products across China. *Remote Sens.* **2021**, *13*, 1208. [CrossRef]
17. Scofield, R.A.; Kuligowski, R.J. Status and Outlook of Operational Satellite Precipitation Algorithms for Extreme-Precipitation Events. *Weather Forecast.* **2003**, *18*, 1037–1051. [CrossRef]
18. Hsu, K.; Gao, X.; Sorooshian, S.; Gupta, H.V. Precipitation Estimation from Remotely Sensed Information Using Artificial Neural Networks. *J. Appl. Meteorol. Climatol.* **1997**, *36*, 1176–1190. [CrossRef]
19. Joyce, R.J.; Janowiak, J.E.; Arkin, P.A.; Xie, P. CMORPH: A Method That Produces Global Precipitation Estimates from Passive Microwave and Infrared Data at High Spatial and Temporal Resolution. *J. Hydrometeorol.* **2004**, *5*, 487–503. [CrossRef]
20. Kubota, T.; Shige, S.; Hashizume, H.; Aonashi, K.; Takahashi, N.; Seto, S.; Hirose, M.; Takayabu, Y.N.; Ushio, T.; Nakagawa, K.; et al. Global Precipitation Map Using Satellite-Borne Microwave Radiometers by the GSMaP Project: Production and Validation. *IEEE Trans. Geosci. Remote Sens.* **2007**, *45*, 2259–2275. [CrossRef]
21. Huffman, G.J.; Bolvin, D.T.; Braithwaite, D.; Hsu, K.; Joyce, R.; Kidd, C.; Nelkin, E.J.; Sorooshian, S.; Tan, J.; Xie, P. NASA Global Precipitation Easurement (GPM) Integrated Multi-SatellitE Retrievals for GPM (IMERG). NASA Algorithm Theoretical Basis Doc., Version 06, 38p. Available online: https://pmm.nasa.gov/sites/default/files/document_files/IMERG_ATBD_V06.pdf (accessed on 9 October 2023).
22. Gharanjik, A.; Mishra, K.V.; Bhavani Shankar, M.R.; Ottersten, B. Learning-Based Rainfall Estimation via Communication Satellite Links. In Proceedings of the 2018 IEEE Statistical Signal Processing Workshop (SSP), Freiburg im Breisgau, Germany, 10–13 June 2018; pp. 130–134. [CrossRef]
23. Gharanjik, A.; Bhavani Shankar, M.R.B.; Zimmer, F.; Ottersten, B. Centralized Rainfall Estimation Using Carrier to Noise of Satellite Communication Links. *IEEE J. Sel. Areas Commun.* **2018**, *36*, 1065–1073. [CrossRef]
24. Tardieu, J.; Leroy, M. Radome, le réseau temps réel d'observation au sol de Météo-France. *La Météorologie* **2003**, *40*, 40–43. [CrossRef]
25. Guillou, Y. L'automatisation des observations météorologiques de surface à Météo-France. Une r-évolution. *La Météorologie* **2018**, *100*, 96–99. [CrossRef]
26. Tabary, P. The New French Operational Radar Rainfall Product. Part I: Methodology. *Weather Forecast.* **2007**, *22*, 393–408. [CrossRef]
27. Figueras i Ventura, J.; Tabary, P. The New French Operational Polarimetric Radar Rainfall Rate Product. *J. Appl. Meteorol. Climatol.* **2013**, *52*, 1817–1835. [CrossRef]
28. Saltikoff, E.; Haase, G.; Delobbe, L.; Gaussiat, N.; Martet, M.; Idziorek, D.; Leijnse, H.; Novák, P.; Lukach, M.; Stephan, K. OPERA the Radar Project. *Atmosphere* **2019**, *10*, 320. [CrossRef]
29. Le Bastard, T.; Caumont, O.; Gaussiat, N.; Karbou, F. Combined Use of Volume Radar Observations and High-Resolution Numerical Weather Predictions to Estimate Precipitation at the Ground: Methodology and Proof of Concept. *Atmos. Meas. Tech.* **2019**, *12*, 5669–5684. [CrossRef]

30. Chochon, R.; Martin, N.; Lebourg, T.; Vidal, M. Analysis of Extreme Precipitation during the Mediterranean Event Associated with the Alex Storm in the Alpes-Maritimes: Atmospheric Mechanisms and Resulting Rainfall. In Proceedings of the SimHydro 2021: Models for Complex and Global Water Issues, Nice, France, 16–18 June 2021; Available online: https://hal.science/hal-03374712 (accessed on 9 October 2023).
31. Qiu, Y. Multiscale Assessment of Hydrological Responses of Nature-Based Solutions to Improve Urban Resilience. Ph.D. Thesis, École des Ponts ParisTech, Champs-sur-Marne, France, 2021. Available online: https://pastel.hal.science/tel-03404617 (accessed on 9 October 2023).
32. Park, S.; Berenguer, M.; Sempere-Torres, D. Long-Term Analysis of Gauge-Adjusted Radar Rainfall Accumulations at European Scale. *J. Hydrol.* **2019**, *573*, 768–777. [CrossRef]
33. Nguyen, P.; Shearer, E.J.; Ombadi, M.; Afzali Gorooh, V.; Hsu, K.; Sorooshian, S.; Logan, W.S.; Ralph, M. PERSIANN Dynamic Infrared–Rain Rate Model (PDIR) for High-Resolution, Real-Time Satellite Precipitation Estimation. *Bull. Am. Meteorol. Soc.* **2020**, *101*, E286–E302. [CrossRef]
34. Arkin, P.A.; Meisner, B.N. The Relationship between Large-Scale Convective Rainfall and Cold Cloud over the Western Hemisphere during 1982-84. *Mon. Weather Rev.* **1987**, *115*, 51–74. [CrossRef]
35. Berthomier, L.; Perier, L. Espresso: A Global Deep Learning Model to Estimate Precipitation from Satellite Observations. *Meteorology* **2023**, *2*, 421–444. [CrossRef]
36. Shamir, E.; Rimmer, A.; Georgakakos, K.P. The Use of an Orographic Precipitation Model to Assess the Precipitation Spatial Distribution in Lake Kinneret Watershed. *Water* **2016**, *8*, 591. [CrossRef]
37. Hobouchian, M.P.; Salio, P.; Skabar, Y.G.; Vila, D.; Garreaud, R. Assessment of Satellite Precipitation Estimates over the Slopes of the Subtropical Andes. *Atmos. Res.* **2017**, *190*, 43–54. [CrossRef]
38. Georgakakos, K.; Modrick, T.; Spencer, C. Operational Microwave-Adjusted Hydro-Estimator to Support Flash Flood Assessments Worldwide. In Proceedings of the AGU Fall Meeting 2021, New Orleans, LA, USA, 13–17 December 2021; p. H13H-01. Available online: https://ui.adsabs.harvard.edu/abs/2021AGUFM.H13H..01G (accessed on 9 October 2023).
39. Nguyen, P.; Ombadi, M.; Afzali Gorooh, V.; Shearer, E.J.; Sadeghi, M.; Sorooshian, S.; Hsu, K.; Bolvin, D.; Ralph, M.F. PERSIANN Dynamic Infrared–Rain Rate (PDIR-Now): A Near-Real-Time, Quasi-Global Satellite Precipitation Dataset. *J. Hydrometeorol.* **2020**, *21*, 2893–2906. [CrossRef]
40. Hong, Y.; Hsu, K.-L.; Sorooshian, S.; Gao, X. Precipitation Estimation from Remotely Sensed Imagery Using an Artificial Neural Network Cloud Classification System. *J. Appl. Meteorol. Climatol.* **2004**, *43*, 1834–1853. [CrossRef]
41. Fick, S.E.; Hijmans, R.J. WorldClim 2: New 1-Km Spatial Resolution Climate Surfaces for Global Land Areas. *Int. J. Climatol.* **2017**, *37*, 4302–4315. [CrossRef]
42. Ashouri, H.; Hsu, K.-L.; Sorooshian, S.; Braithwaite, D.K.; Knapp, K.R.; Cecil, L.D.; Nelson, B.R.; Prat, O.P. PERSIANN-CDR: Daily Precipitation Climate Data Record from Multisatellite Observations for Hydrological and Climate Studies. *Bull. Am. Meteorol. Soc.* **2015**, *96*, 69–83. [CrossRef]
43. Kummerow, C.D. Introduction to Passive Microwave Retrieval Methods. In *Satellite Precipitation Measurement: Volume 1*; Levizzani, V., Kidd, C., Kirschbaum, D.B., Kummerow, C.D., Nakamura, K., Turk, F.J., Eds.; Advances in Global Change Research; Springer International Publishing: Cham, Switzerland, 2020; pp. 123–140. [CrossRef]
44. Kidd, C.; Matsui, T.; Blackwell, W.; Braun, S.; Leslie, R.; Griffith, Z. Precipitation Estimation from the NASA TROPICS Mission: Initial Retrievals and Validation. *Remote Sens.* **2022**, *14*, 2992. [CrossRef]
45. Battaglia, A.; Kollias, P.; Dhillon, R.; Roy, R.; Tanelli, S.; Lamer, K.; Grecu, M.; Lebsock, M.; Watters, D.; Mroz, K.; et al. Spaceborne Cloud and Precipitation Radars: Status, Challenges, and Ways Forward. *Rev. Geophys.* **2020**, *58*, e2019RG000686. [CrossRef] [PubMed]
46. Watters, D.; Battaglia, A.; Mroz, K.; Tridon, F. Validation of the GPM Version-5 Surface Rainfall Products over Great Britain and Ireland. *J. Hydrometeorol.* **2018**, *19*, 1617–1636. [CrossRef]
47. Joyce, R.J.; Xie, P.; Yarosh, Y.; Janowiak, J.E.; Arkin, P.A. CMORPH: A “Morphing” Approach for High Resolution Precipitation Product Generation. In *Satellite Rainfall Applications for Surface Hydrology*; Gebremichael, M., Hossain, F., Eds.; Springer: Dordrecht, The Netherlands, 2010; pp. 23–37. [CrossRef]
48. Ushio, T.; Sasashige, K.; Kubota, T.; Shige, S.; Okamoto, K.; Aonashi, K.; Inoue, T.; Takahashi, N.; Iguchi, T.; Kachi, M.; et al. A Kalman Filter Approach to the Global Satellite Mapping of Precipitation (GSMaP) from Combined Passive Microwave and Infrared Radiometric Data. *J. Meteorol. Soc. Japan. Ser. II* **2009**, *87A*, 137–151. [CrossRef]
49. Kubota, T.; Aonashi, K.; Ushio, T.; Shige, S.; Takayabu, Y.N.; Kachi, M.; Arai, Y.; Tashima, T.; Masaki, T.; Kawamoto, N.; et al. Global Satellite Mapping of Precipitation (GSMaP) Products in the GPM Era. In *Satellite Precipitation Measurement: Volume 1*; Levizzani, V., Kidd, C., Kirschbaum, D.B., Kummerow, C.D., Nakamura, K., Turk, F.J., Eds.; Advances in Global Change Research; Springer International Publishing: Cham, Switzerland, 2020; pp. 355–373. [CrossRef]
50. Shi, J.; Wang, B.; Wang, G.; Yuan, F.; Shi, C.; Zhou, X.; Zhang, L.; Zhao, C. Are the Latest GSMaP Satellite Precipitation Products Feasible for Daily and Hourly Discharge Simulations in the Yellow River Source Region? *Remote Sens.* **2021**, *13*, 4199. [CrossRef]
51. Ramadhan, R.; Marzuki, M.; Yusnaini, H.; Muharsyah, R.; Tangang, F.; Vonnisa, M.; Harmadi, H. A Preliminary Assessment of the GSMaP Version 08 Products over Indonesian Maritime Continent against Gauge Data. *Remote Sens.* **2023**, *15*, 1115. [CrossRef]
52. O, S.; Foelsche, U.; Kirchengast, G.; Fuchsberger, J.; Tan, J.; Petersen, W.A. Evaluation of GPM IMERG Early, Late, and Final Rainfall Estimates Using WegenerNet Gauge Data in Southeastern Austria. *Hydrol. Earth Syst. Sci.* **2017**, *21*, 6559–6572. [CrossRef]

53. Mishra, K.V.; Gharanjik, A.; Bhavani Shankar, M.R.; Ottersten, B. *Deep Learning Framework for Precipitation Retrievals from Communication Satellites*; Ede-Wageningen: Ede, The Netherlands, 2018.
54. Mishra, K.V.; Chandrasekar, V.; Nguyen, C.; Vega, M. The Signal Processor System for the NASA Dual-Frequency Dual-Polarized Doppler Radar. In Proceedings of the 2012 IEEE International Geoscience and Remote Sensing Symposium, Munich, Germany, 22–27 July 2012; pp. 4774–4777. [CrossRef]
55. Zhang, X.; Lu, X.; Wang, X. Comparison of Spatial Interpolation Methods Based on Rain Gauges for Annual Precipitation on the Tibetan Plateau. *Pol. J. Environ. Stud.* **2016**, *25*, 1339–1345. [CrossRef] [PubMed]
56. Thiessen, A.H. Precipitation averages for large areas. *Mon. Weather Rev.* **1911**, *39*, 1082–1089. [CrossRef]
57. Vicente-Serrano, S.M.; Saz-Sánchez, M.A.; Cuadrat, J.M. Comparative Analysis of Interpolation Methods in the Middle Ebro Valley (Spain): Application to Annual Precipitation and Temperature. *Clim. Res.* **2003**, *24*, 161–180. [CrossRef]
58. Lebrenz, H.; Bárdossy, A. Geostatistical Interpolation by Quantile Kriging. *Hydrol. Earth Syst. Sci.* **2019**, *23*, 1633–1648. [CrossRef]
59. Saemian, P.; Hosseini-Moghari, S.-M.; Fatehi, I.; Shoarinezhad, V.; Modiri, E.; Tourian, M.J.; Tang, Q.; Nowak, W.; Bárdossy, A.; Sneeuw, N. Comprehensive Evaluation of Precipitation Datasets over Iran. *J. Hydrol.* **2021**, *603*, 127054. [CrossRef]
60. Thiemig, V.; Rojas, R.; Zambrano-Bigiarini, M.; Levizzani, V.; Roo, A.D. Validation of Satellite-Based Precipitation Products over Sparsely Gauged African River Basins. *J. Hydrometeorol.* **2012**, *13*, 1760–1783. [CrossRef]
61. Zambrano-Bigiarini, M.; Nauditt, A.; Birkel, C.; Verbist, K.; Ribbe, L. Temporal and Spatial Evaluation of Satellite-Based Rainfall Estimates across the Complex Topographical and Climatic Gradients of Chile. *Hydrol. Earth Syst. Sci.* **2017**, *21*, 1295–1320. [CrossRef]
62. Llauca, H.; Lavado-Casimiro, W.; León, K.; Jimenez, J.; Traverso, K.; Rau, P. Assessing Near Real-Time Satellite Precipitation Products for Flood Simulations at Sub-Daily Scales in a Sparsely Gauged Watershed in Peruvian Andes. *Remote Sens.* **2021**, *13*, 826. [CrossRef]
63. Hersbach, H.; Bell, B.; Berrisford, P.; Hirahara, S.; Horányi, A.; Muñoz-Sabater, J.; Nicolas, J.; Peubey, C.; Radu, R.; Schepers, D.; et al. The ERA5 Global Reanalysis. *Q. J. R. Meteorol. Soc.* **2020**, *146*, 1999–2049. [CrossRef]
64. Afzali Gorooh, V.; Shearer, E.J.; Nguyen, P.; Hsu, K.; Sorooshian, S.; Cannon, F.; Ralph, M. Performance of New Near-Real-Time PERSIANN Product (PDIR-Now) for Atmospheric River Events over the Russian River Basin, California. *J. Hydrometeorol.* **2022**, *23*, 1899–1911. [CrossRef]
65. Huang, W.-R.; Liu, P.-Y.; Hsu, J. Multiple Timescale Assessment of Wet Season Precipitation Estimation over Taiwan Using the PERSIANN Family Products. *Int. J. Appl. Earth Obs. Geoinf.* **2021**, *103*, 102521. [CrossRef]
66. Rachdane, M.; Khalki, E.M.E.; Saidi, M.E.; Nehmadou, M.; Ahbari, A.; Tramblay, Y. Comparison of High-Resolution Satellite Precipitation Products in Sub-Saharan Morocco. *Water* **2022**, *14*, 3336. [CrossRef]
67. Hisam, E.; Danandeh Mehr, A.; Alganci, U.; Zafer Seker, D. Comprehensive Evaluation of Satellite-Based and Reanalysis Precipitation Products over the Mediterranean Region in Turkey. *Adv. Space Res.* **2023**, *71*, 3005–3021. [CrossRef]
68. Bieliński, T. A Parallax Shift Effect Correction Based on Cloud Height for Geostationary Satellites and Radar Observations. *Remote Sens.* **2020**, *12*, 365. [CrossRef]
69. Schleiss, M.; Olsson, J.; Berg, P.; Niemi, T.; Kokkonen, T.; Thorndahl, S.; Nielsen, R.; Ellerbæk Nielsen, J.; Bozhinova, D.; Pulkkinen, S. The Accuracy of Weather Radar in Heavy Rain: A Comparative Study for Denmark, the Netherlands, Finland and Sweden. *Hydrol. Earth Syst. Sci.* **2020**, *24*, 3157–3188. [CrossRef]
70. Di Curzio, D.; Di Giovanni, A.; Lidori, R.; Montopoli, M.; Rusi, S. Comparing Rain Gauge and Weather RaDAR Data in the Estimation of the Pluviometric Inflow from the Apennine Ridge to the Adriatic Coast (Abruzzo Region, Central Italy). *Hydrology* **2022**, *9*, 225. [CrossRef]
71. Rojas, Y.; Minder, J.R.; Campbell, L.S.; Massmann, A.; Garreaud, R. Assessment of GPM IMERG Satellite Precipitation Estimation and Its Dependence on Microphysical Rain Regimes over the Mountains of South-Central Chile. *Atmos. Res.* **2021**, *253*, 105454. [CrossRef]
72. Giorgi, F.; Torma, C.; Coppola, E.; Ban, N.; Schär, C.; Somot, S. Enhanced Summer Convective Rainfall at Alpine High Elevations in Response to Climate Warming. *Nat. Geosci.* **2016**, *9*, 584–589. [CrossRef]